Journal of Advances in Modeling Earth Systems

RESEARCH ARTICLE
10.1029/2018MS001369

Key Points:
- New CMCC climate model built coupling atmosphere and land components of NCAR model with NEMO ocean model
- Realistic representation of mean climate and main patterns of variability, mostly for the Northern Hemisphere winter
- Improvements in some aspects of the SST pattern with respect to a previous version of CMCC model

Supporting Information:
- Supporting Information S1
- Data Set S1
- Data Set S2
- Data Set S3
- Data Set S4

Correspondence to:
A. Cherchi,
annalisa.cherchi@ingv.it

Citation:
Cherchi, A., Fogli, P. G., Lovato, T., Peano, D., Iovino, D., Gualdi, S., et al. (2019). Global mean climate and main patterns of variability in the CMCC-CM2 coupled model. *Journal of Advances in Modeling Earth Systems*, *11*. https://doi.org/10.1029/2018MS001369

Received 10 MAY 2018
Accepted 7 DEC 2018
Accepted article online 13 DEC 2018

Global Mean Climate and Main Patterns of Variability in the CMCC-CM2 Coupled Model

A. Cherchi[1,2], P. G. Fogli[1], T. Lovato[1], D. Peano[1], D. Iovino[1], S. Gualdi[1,2], S. Masina[1,2], E. Scoccimarro[1], S. Materia[1], A. Bellucci[1], and A. Navarra[1,2]

[1]Fondazione Centro Euro-Mediterraneo sui Cambiamenti Climatici, Bologna, Italy, [2]Istituto Nazionale di Geofisica e Vulcanologia, Bologna, Italy

Abstract Euro-Mediterranean Centre on Climate Change coupled climate model (CMCC-CM2) represents the new family of the global coupled climate models developed and used at CMCC. It is based on the atmospheric, land and sea ice components from the Community Earth System Model coupled with the global ocean model Nucleus for European Modeling of the Ocean. This study documents the model components, the coupling strategy, particularly for the oceanic, atmospheric, and sea ice components, and the overall model ability in reproducing the observed mean climate and main patterns of interannual variability. As a first step toward a more comprehensive, process-oriented, validation of the model, this work analyzes a 200-year simulation performed under constant forcing corresponding to present-day climate conditions. In terms of mean climate, the model is able to realistically reproduce the main patterns of temperature, precipitation, and winds. Specifically, we report improvements in the representation of the sea surface temperature with respect to the previous version of the model. In terms of mean atmospheric circulation features, we notice a realistic simulation of upper tropospheric winds and midtroposphere geopotential eddies. The oceanic heat transport and the Atlantic meridional overturning circulation satisfactorily compare with present-day observations and estimates from global ocean reanalyses. The sea ice patterns and associated seasonal variations are realistically reproduced in both hemispheres, with a better skill in winter. Main weaknesses of the simulated climate are related with the precipitation patterns, specifically in the tropical regions with large dry biases over the Amazon basin. Similarly, the seasonal precipitation associated with the monsoons, mostly over Asia, is weaker than observed. The main patterns of interannual variability in terms of dominant empirical orthogonal functions are faithfully reproduced, mostly in the Northern Hemisphere winter. In the tropics the main teleconnection patterns associated with El Niño–Southern Oscillation and with the Indian Ocean Dipole are also in good agreement with observations.

1. Introduction

The Euro-Mediterranean Centre on Climate Change (CMCC) Foundation is dedicated to the understanding of the global climate variability and climate change, including mechanisms, causes, and impacts. One of the most important activities at CMCC is the development of a global coupled model as the main vehicle for the study of climate. Here we describe the latest version of the CMCC coupled climate model (CMCC-CM2), largely based on the Community Earth System Model (CESM) project (http://www.cesm.ucar.edu) operated at the National Centre for Atmospheric Research (NCAR) in the United States. The important and strategic difference with the NCAR coupled model is the oceanic component. As a member of the Nucleus for European Modelling of the Ocean (NEMO) consortium (https://www.nemo-ocean.eu), CMCC takes an active part in the development and evolution of the ocean related engines. That motivated us in replacing the CESM ocean component with the NEMO physical core. This system constitutes the CMCC Climate Model V2, CMCC-CM2, and it will contribute to the necessary model diversity desired for the upcoming Coupled Model Intercomparison Project phase 6 (CMIP6; Eyring et al., 2016). The model is an essential component of the CMCC seamless simulation system that spans operational seasonal predictions and climate scenarios productions.

CMCC-CM2 represents the base for a family of configurations responding to the different climate needs and applications, including the coupled Climate-Carbon cycle studies through the setup of an Earth System Model (CMCC-ESM 2), a twin set of configurations (CMCC-CM2-HR4 and CMCC-CM2-VHR4), specifically developed for the HighResMIP protocol (Haarsma et al., 2016), and the seasonal prediction system and its

operational framework (Sanna et al., 2015). The model is an evolution of the CMCC-CM model (Scoccimarro et al., 2011) used within the fifth CMIP (CMIP5; Taylor et al., 2012). CMCC-CM has been an update of the SINTEX-G (Scale Interaction Experiment) model (Bellucci et al., 2008; Cherchi et al., 2008; Gualdi et al., 2008) used for the CMIP3 (Meehl et al., 2007) effort. Compared to the previous model versions, CMCC-CM2 includes upgraded physics of the ocean, sea ice, atmosphere and land components as well as an advanced coupling environment (see section 2.1 for more details).

A thorough validation of a state of the art coupled model requires an extensive documentation, as well as a large set of experiments. This study is the first step toward a more comprehensive assessment of the CMCC new climate model, evaluating the simulated mean state and internal variability of the climate system. Specifically, here a first assessment is given of the model ability in reproducing the present-day mean climate and variability in terms of the main tropical and extratropical patterns. To do this, an extended simulation using constant present-day climate forcing is analyzed and validated against recent-era observations and reanalyses data sets. A long control experiment with present-day constant atmospheric forcing is suitable for the assessment of the mean climate and main patterns of variability in a global coupled model. A similar approach has been followed in a number of previous climate model assessments (see, among the others, Morgenstern et al., 2009; Delworth et al., 2012; Small et al., 2014; Rackow et al., 2018). In fact, unlike standard CMIP control (preindustrial) experiments, present-day simulations allow a direct comparison with recent-era observations and reanalyses. Also, compared to standard CMIP historical simulations, a present-day climate simulation is not expected to yield qualitatively different results, at least in terms of mean climate and main patterns of interannual variability.

This work is organized as follows: section 2 describes the coupled model components as well as the details of the experiment used in this evaluation, and the data sets/reanalyses used as references. The evaluation and validation of the model is then organized into the analysis of the mean state in section 3 and of the main patterns of variability in section 4. Finally, section 5 reports a summary of the CMCC-CM2 performance.

2. Model and Data Description

2.1. CMCC-CM2 Climate Model

The CMCC-CM2 model components are full 3-D dynamical models, communicating via a coupler (CPL v7; Craig et al., 2012) that synchronizes the exchange of fields among the different model constituents. The coupling architecture provides plug and play capabilities of data and active components. It includes scripting system and informative timing utilities. The components of the coupled model are the Community Atmosphere Model (CAM v5, except for the HighResMIP configurations, for which v4 is used), the NEMO ocean engine (v3.6), the Community sea-Ice CodE (CICE v4) and the Community Land Model (CLM v4.5). In CMCC-CM2 all model components have a coupling frequency of 30 min, except for the ocean that exchanges coupling fields every hour (equal to the relative integration time step). This setting has been selected so as to achieve the highest coupling frequency among model components. A thorough description of the coupling strategy between NEMO and both atmospheric and sea ice NCAR models is given in Fogli and Iovino (2014), while relevant information for each component of the coupled model are reported below.

2.1.1. Atmosphere

The atmospheric component of CMCC-CM2 is the CAM in its version 5 (CAM5, Neale et al., 2012). Physical processes have been substantially improved in CAM5 compared to previous versions and it represents the first version able to simulate the cloud-aerosol indirect radiative effects. Specifically, compared to previous versions, CAM5 has (i) a new moist turbulence scheme to explicitly simulate stratus-radiation-turbulence interactions thus taking into account the full aerosols indirect effects within stratus (Bretherthon & Park, 2009); (ii) a new shallow convection scheme to accurately simulate the spatial distribution of the shallow convective activity (Park & Bretherton, 2009); (iii) prognostic, two-moment formulation for cloud droplets and cloud ice to represent stratiform microphysical processes (Gettelman et al., 2008); (iv) a revised cloud macrophysics scheme to provide a more transparent treatment of cloud processes (Park et al., 2014); (v) a new three-mode modal aerosols scheme providing internally mixed representations of number concentrations and mass for Aitken, accumulation and coarse aerosols modes (Liu et al., 2012); and (vi) an updated radiation scheme (Iacono et al., 2008). In this new version of CAM the aerosols module is fully interactive, with emissions of

biogenic compounds and deposition of aerosols to snow, ice, ocean, and vegetation handled through the coupler.

The dynamical core of the atmosphere model can be either finite-volume (FV) or based on spectral elements. In CMCC-CM2 we use the FV dynamical core where discretization is local and entirely in physical space. The horizontal discretization is based on a conservative "flux-form semi-Lagrangian" scheme (Lin & Rood, 1996). The vertical discretization is semi-Lagrangian with a conservative remapping. The FV dynamics and physics are time split as all the prognostic variables are updated sequentially by the dynamics and then by the physics (Neale et al., 2012). The time integration within the FV dynamics is fully explicit, with subcycling within the 2-D Lagrangian dynamics to stabilize the fastest waves. The transport of tracers can take a much larger time with respect to the dynamics time step, up to the physics time step (30 min).

In CMCC-CM2, CAM5 is used at a horizontal resolution of about 1°, with a regular grid of 0.9° × 1.25°. The default vertical structure of CAM consists of 30 vertical hybrid levels with about 1.2 km of vertical spacing throughout the free troposphere and the lower stratosphere (17 levels are below 200 hPa). The model top is at 2 hPa (Richter et al., 2014). Following CMIP5 models classification of low-top and high-top models as in Charlton-Perez et al. (2013), CMCC-CM2 would belong to the upper bound of low-top models.

The atmosphere sends to the coupler information about zonal and meridional velocities, atmospheric temperature and humidity, including precipitation, and downward shortwave and longwave radiation. It receives from the coupler status of the surface albedo, land/ice/ocean fractions, sea surface temperature (SST), surface wind stresses, sensible and latent heat fluxes, upward longwave radiation, evaporation, and dust emissions.

2.1.2. Ocean

The ocean general circulation in CMCC-CM2 is based on the European modeling framework NEMO (v3.6; Madec & the NEMO team, 2016) that here accounts for the physical circulation engine (OPA, Océan Parallélisé) and the interface to compute the transport of oceanic tracers (TOP, Tracer in the Ocean Paradigm). NEMO is a flexible tool for the study of the ocean and its interactions with the other components of the Earth climate system over a wide range of space and time scales. The physical engine of NEMO resolves the classic primitive equations of ocean circulation subject to the Boussinesq, hydrostatic and incompressibility approximations. The prognostic variables are the three velocity components, the sea surface height, the potential seawater temperature, and salinity. Time integration is performed using a modified Robert-Asselin filtered leapfrog for nondiffusive processes and a forward (backward) scheme for horizontal (vertical) diffusive processes, and the time step used is 60 min. The horizontal space is discretized on a staggered grid (Arakawa C type) masked over land areas, while in the vertical it is possible to use geopotential, terrain-following coordinates, or a hybrid combination of the two. NEMO ocean engine offers a wide range of numerical schemes to solve key physical processes, such as advection, diffusion, vertical dynamics, seawater equation of state, lateral and bottom boundaries, and air-sea interactions.

In CMCC-CM2, the ocean component uses the tripolar ORCA grid based on Mercator projection (Madec & Imbard, 1996) with a horizontal resolution of about 1°, with a varying latitudinal resolution ranging from 1/3° near the equator up to 1° at high latitudes. In the vertical 50 geopotential levels, ranging from 1 to 400 m, are considered. The adopted linear free-surface formulation (Roullet & Madec, 2000) allows computing fluxes of volume, tracers, and momentum using fixed reference ocean surface height. This configuration uses the United Nations Educational, Scientific and Cultural Organization nonlinear equation of state (Fofonoff & Millard, 1983). Advection of tracers is performed with the Total Variance Dissipation scheme, while momentum advection is formulated in vector invariant form using an energy-conserving scheme (Zalesak, 1979). The vertical physics is parameterized using the turbulent kinetic energy closure scheme (Blanke & Delecluse, 1993) plus parameterizations of double diffusion, Langmuir cell, and surface wave breaking. An enhanced vertical diffusion parameterization is used in regions where the stratification becomes unstable. Tracers lateral diffusion uses a diffusivity coefficient scaled according to the grid spacing and is parameterized by an isoneutral Laplacian operator. An additional eddy-induced velocity is also computed with a spatially and temporally varying coefficient. Lateral viscosity uses a space-varying coefficient and is parameterized by a horizontal Laplacian operator. Free-slip boundary conditions are applied at the ocean lateral boundaries, while a bottom intensified tidally driven mixing, a diffusive bottom boundary layer scheme, and a nonlinear bottom friction are applied at the ocean floor.

The shortwave radiation from the atmosphere is absorbed in the surface layers using three-band chlorophyll-dependent attenuation coefficients (Lengaigne et al., 2007).

The ocean model requires fluxes of momentum, heat, and freshwater at the air-sea interface as surface boundary conditions, which are provided by the other components of the CMCC-CM2 through the coupler. The selected 1-hr air-sea coupling frequency is high enough to resolve the diurnal cycle in the ocean.

2.1.3. Sea Ice

The sea ice component is the Community Ice CodE in its version 4 (CICE4; Hunke & Lipscomb, 2008). CICE4 includes several interactive components: the thermodynamics that computes local growth rates of snow and ice due to vertical conductive, radiative, and turbulent fluxes, including snowfall (Bitz & Lipscomb, 1999), the ice dynamics to predicts the velocity field of the ice pack based on elastic-viscous-plastic properties (Hunke & Dukowicz, 2002), the transport for the advection of the areal concentration, ice volume and other state variables, and a subgrid-scale representation of the ice thickness distribution following Thorndike et al. (1975) and Rothrock (1975). For each category, state variables in CICE4 include ice fraction, ice and snow volumes, ice and snow energy (for each layer), surface temperature, and ice age. In CMCC-CM2 we use five categories of sea ice thickness with lower bounds at 0, 0.64, 1.39, 2.47, and 4.57 m following the original category boundary formula. CICE4 also includes a multiple-scattering shortwave radiation treatment (Briegleb & Light, 2007) and is able to simulate explicitly melt pond evolution and the deposition and cycling of aerosols (dust and black carbon) within the ice pack (Holland et al., 2012). In CMCC-CM2 CICE4 is used with a time step of 30 min. The thermodynamic model has one layer of snow and four layers of ice in each of the five ice thickness categories.

In CMCC-CM2, CICE shares the same horizontal grid of the ocean component. Sea surface and near-surface air properties (temperature, salinity, humidity, and heat) are exchanged between the sea ice model and the atmosphere/ocean models through the coupler. An alternative to CICE could have been to use LIM (Louvain-La-Neuve Ice Model; Vancoppenolle et al., 2012), which is implemented as a module inside NEMO, but it is not designed as stand-alone model, and it would have needed important changes to be compliant with CESM philosophy, that is, to communicate directly with the coupler and compute the surface fluxes to be sent to the atmosphere.

2.1.4. Land Surface Processes

The land component is the CLM. CLM is designed to represent and enable the study of the physical, chemical, and biological processes by which terrestrial ecosystems affect and are affected by climate across a variety of spatial and temporal scales.

CMCC-CM2 implements the CLM version 4.5 model (CLM4.5; Oleson et al., 2013), sharing the same horizontal grid used in the atmospheric component. In CLM4.5 several parameterizations have been revised to reflect new scientific understanding and to reduce biases identified in previous versions, like low soil carbon stocks in the Arctic, unrealistically high leaf area index in the tropics, and a transient twentieth century carbon response that was inconsistent with observational estimates (Koven et al., 2013). In particular, among the main improvements in CLM4.5, an update of canopy processes, including a revised canopy radiation scheme and canopy scaling of leaf processes (Bonan et al., 2011), temperature acclimation of photosynthesis, and improved stability of the iterative solution in the photosynthesis and stomatal conductance model (Sun et al., 2012), can be listed. The hydrology processes list modifications related with treatment of icy permafrost ground (Swenson et al., 2012) and improve the simulation of snow cover fraction (Swenson & Lawrence, 2012), by separating the processes governing snowmelt (i.e., depletion) and snowfall (i.e., accumulation).

The fire parameterization in CLM4.5 accounts for four components: (1) nonpeat fires outside cropland and tropical forest, (2) agricultural fires, (3) peat fires, and (4) deforestation fires in tropical closed forest (Li et al., 2012, 2013). The original deforestation-fire parameterization was set to account for land use changes and deforestation rate, but this configuration leads to a mistakenly large fire extension under dry climate conditions (i.e., in the Amazon region). After updating the deforestation-fire parameterization, the simulated burned area in the tropical closed forests reached reasonable extensions (Li et al., 2014).

In CMCC-CM2, land carbon (C) and nitrogen (N) cycles are activated with the idea to have a better representation of the land surface and vegetation, with a more realistic interaction with the atmosphere. However, the dynamic vegetation module is not active: vegetation can grow, shrink, or die thanks to the interaction with climate and nutrients, but plant functional types, representing vegetation types in each grid cell, are

constant. Thus, vegetation types cannot change in response to modified climate conditions. The newly introduced carbon and nitrogen cycling of the Century soil model (Parton et al., 1988) includes pool with long turnover timescales, the longest being of the order of hundreds of years, and they are vertically resolved in the soil layers. For this reason, the land model is initialized independently from the other components using the results of a long spinup simulation performed in offline mode in order to reach the equilibrium for the soil pools. Such a long spinup is necessary to avoid the occurrence of spurious trends that would corrupt the results of the coupled simulations. We applied the model initialization technique as described by Koven et al. (2013). This method consists of two phases: a first 1,020-year simulation, in which each N and C pool are accelerated by a different degree (i.e., the slowest pools are accelerated more than the fast ones) leading all the pools to an approximate annual turnover timescale and a second 300-year simulation in which the acceleration is deactivated in order to bring back each pool to its real turnover timescale. More details on the terrestrial carbon properties, including trends, and more details of the biogeochemical cycles will be included in a forthcoming work with the validation of the CMCC Earth System Model.

CLM is coupled with the River Transport Model (RTM), which routes liquid and ice runoff from the land surface model to the active ocean thus enabling for a closed hydrologic cycle (Branstetter, 2001; Branstetter & Famiglietti, 1999). The RTM linearly transports water from each cell to its downstream neighboring cell, with a time-constant flow velocity that only depends on the grid cell mean topographic slope. RTM runs at a regular 0.5° resolution with a 3-hr time step, thus longer than that of CLM (30 min) due to computational constraints. Finally, CLM4.5 includes a completely revised and more realistic lake model (Subin et al., 2012).

2.2. CMCC-CM2 Standard Configuration and Experiment Setup

The CMCC-CM2 standard configuration, namely, CMCC-CM2-SR5, uses about 1° horizontal resolution grids for all the components of the system except for the RTM model that, as described above, has a resolution of 0.5°. Alternative configurations, including an eddy-permitting (1/4°) ocean component coupled to a 1° (CMCC-CM2-HR4) and a 1/4° (CMCC-CM2-VHR4) global atmosphere, respectively, have been developed to comply with the CMIP6 HighResMIP effort (Haarsma et al., 2016). For these configurations version 4 of the CAM model (CAM4; Neale et al., 2010) is used with a prescribed aerosols physics. This choice had two major advantages: (i) it allowed a substantial reduction of computational costs, especially beneficial for the high-resolution (CMCC-CM2-VHR4) experiments, and (ii) it made possible the implementation of the MACv2-SP "simple plume" scheme for the anthropogenic aerosols (Stevens et al., 2017) following the HighResMIP protocol.

In CMCC-CM2 the surface topography is obtained from the 30-arc sec global digital elevation model from the U.S. Geological Survey (see Lauritzen et al., 2015), while the ocean bathymetry results from the combination of the ETOPO2 (NOAA, 2006) and IBSCO (Arndt et al., 2013) databases.

The CMCC-CM2 experiment described in this study has present-day (year 2000) forcing conditions with a constant solar irradiance of 1366 W/m^2, a mean seafloor geothermal heat flux of 65 mW/m^2, and fixed greenhouse gases concentrations (i.e., CO_2 = 367 ppm; CH_4 = 1,760 ppb; CFC11 = 653.45 ppt; CFC12 = 535 ppt).

The ocean initial conditions for seawater temperature and salinity were derived from the 2013 World Ocean Atlas (Locarnini et al., 2013; Zweng et al., 2013) and homogeneous sea ice concentrations were set for ice coverage typical of boreal winter. The land component is initialized with the spinup procedure described in the previous section. About 200 years of present-day simulation are completed. The length of the experiment largely allows for investigation of interannual variability. The last 30 years of simulation are used to compute the mean climatologies described in section 3.

The length of the experiment is also sufficient to obtain a balance of fluxes at the ocean and land surfaces as well as at the top of the atmosphere. In fact, the net radiative fluxes at the top of the atmosphere (TOA) stabilize after about 60 years of simulation to a mean value of about 0.3 W/m^2 (see Table 1), which is a satisfactory residual value for a present-day constant forcing simulation (i.e., Delworth et al., 2012; Small et al., 2014). When increasing atmospheric concentration, pathways are considered a global energy imbalance at TOA is expected. Over the past decades estimates have been found to range from 0.5 to 1.0 W/m^2 (Trenberth et al., 2014). Close to the surface (2 m) the global annual mean temperature drops by about 0.4 °C in the first 20 years of simulation and then quickly recovers (Figure 1a) reaching the stable value of about 14.0 °C (see also Table 1). The global annual mean SST drops by about 0.25 °C from the initial condition value in the first 10 years of simulation and then recovers (Figure 1b) reaching equilibrium at about 20.3 °C

Table 1
Global Values and Specific Metrics of Climatic Relevance for CMCC-CM2 Compared With Available Observations (the Data Sets or Reanalysis Used as Observed Values Are Specified in Brackets)

Variables and Metrics	Unit	CMCC-CM2	Observations
TOA balance[a]	W/m^2	0.3	
T2M[b]	°C	14.0	14.4 (ERA-Interim)
T2M-land[c]	°C	12.7	13.5 (CRU); 13.2 (ERA-Interim)
SST[d]	°C	20.3	20.5 (HadISST)
PRECT[e]	mm/d	3.3	2.7 (GPCP)
ITCZ[f]	°N	6–9	6 (GPCP)
NHT[g]	PW	1.79	1.7 ± 0.3 (ERBE/CERES)
MHT[h]	PW	1.08	1.31 ± 0.40 (RAPID/MOCHA)
AMOC[i]	Sv	19.4 ± 2.3	17.0 ± 3.6 (RAPID/MOCHA)

Note. For the model, mean values refer to the last 30 years of simulation. In ERA-Interim, CRU, GPCP, and HadISST, mean values refer to the reference period (1990–2010). CMCC-CM2 = Euro-Mediterranean Centre on Climate Change coupled climate model; GPCP = Global Precipitation Climatology Project.
[a]Radiative balance at top of the atmosphere (TOA) in terms of global annual mean radiative fluxes (incoming minus outgoing). [b]Global annual mean temperature at 2 m (T2M). [c]Global annual mean temperature at 2 m, but the average is over land points only. [d]Global annual sea surface temperature (SST). [e]Global annual mean precipitation (PRECT). [f]position of the Intertropical Convergence Zone (ITCZ) in degrees north measured as the location (latitude) of the maximum precipitation over all longitudes. [g]Peak of global northward ocean heat transport (NHT). [h]Mean Atlantic heat transport (MHT). [i]Value of the annual mean Atlantic meridional overturning circulation (AMOC) measured at 26.5°N.

(see also Table 1). This SST value is computed without taking into account the SST below sea ice, to make it comparable with the HadISST SST data set (Rayner et al., 2003).

2.3. Data Sets and Reanalyses for Comparison

The model performance is assessed by means of the following data sets. Precipitation is taken from the Global Precipitation Climatology Project (GPCP version 2.2; Adler et al., 2003) data set at 2.5° resolution for the period 1979–2005. Monthly mean SST is taken from the HadISST data set (Rayner et al., 2003), while temperature at 2 m is derived from the Climatic Research Unit (CRU) data set (Harris & Jones, 2017). Other atmospheric fields, such as sea level pressure, geopotential height, and wind, come from the ERA-Interim reanalysis (Dee et al., 2011). In the observations/reanalyses the reference period used for the climatology is 1990–2010. To show differences between model and observations all the data are interpolated on the model grid. Sea ice extent is compared with the climatology (1979–2009) provided by the National Snow and Ice Data Center (NSIDC) (Fetterer et al., 2008), available through the website http://nsidc.org/data/docs/noaa/g02135_seaice_index/index.html#processingstep.

3. Global Mean Climate

The annual mean near-surface temperature averaged over the globe in the reference period (1990–2010) is about 14.4 °C, as computed from the ERA-Interim. In the model this value is realistically reproduced (about 14.0 °C; see Table 1) with a global bias of about 0.4 °C. In terms of annual mean the main bias is negative in the Northern Hemisphere high latitudes and slightly positive in the Southern Hemisphere (not shown). Boreal winter climatology shows a cold systematic error in most of the continental

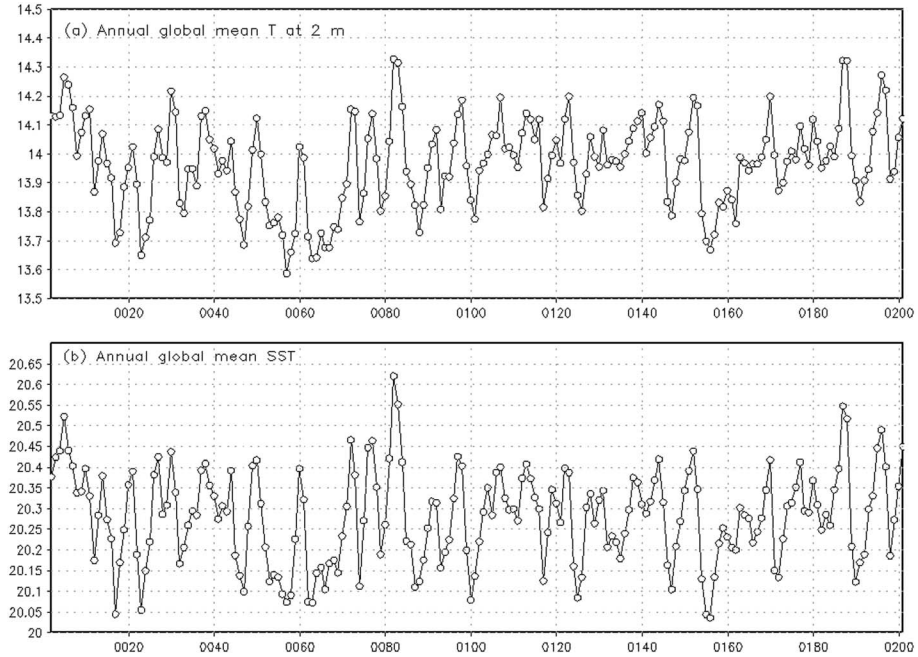

Figure 1. Time series of (a) annual global mean temperature at 2 m (°C) and (b) annual mean global SST (°C) in Euro-Mediterranean Centre on Climate Change coupled climate model present-day control experiment. SST = sea surface temperature.

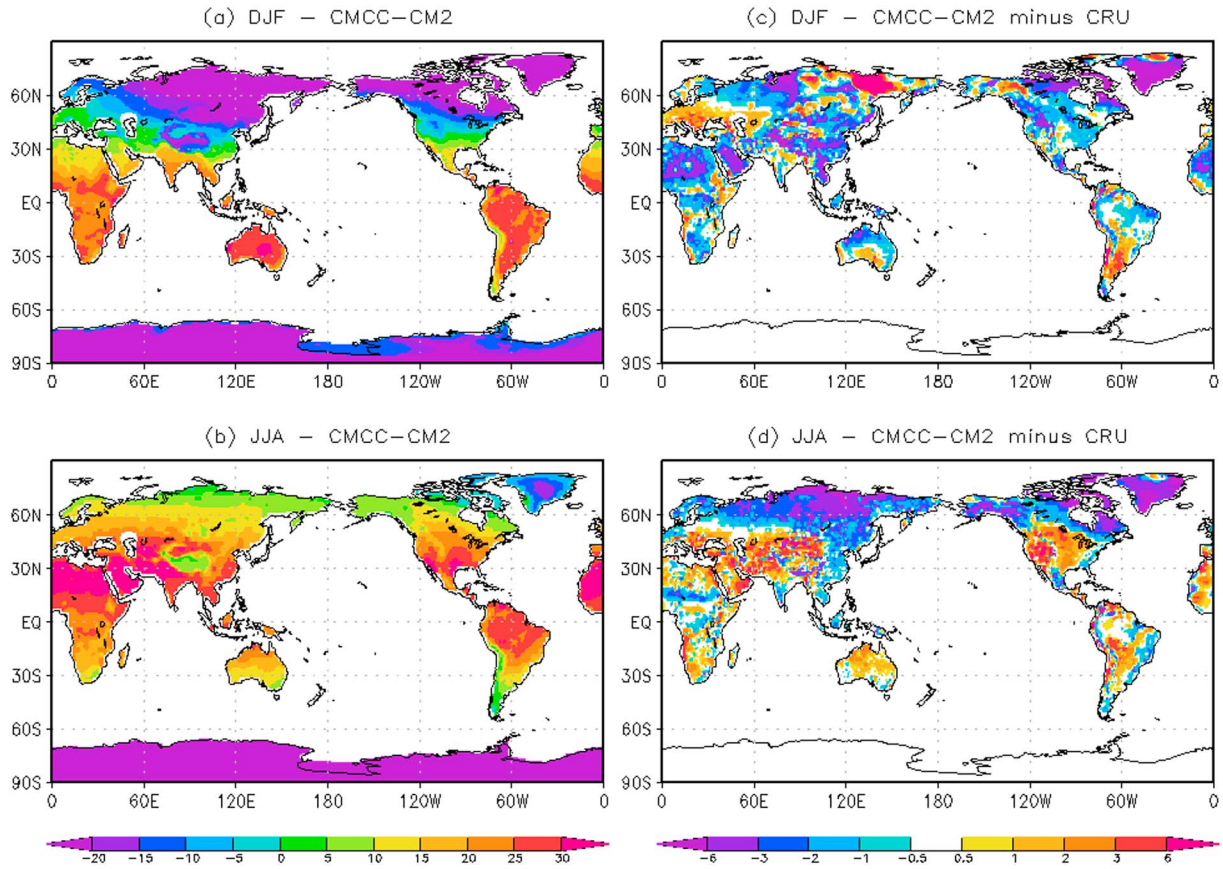

Figure 2. Temperature (°C) at 2 m (land only) averaged in a boreal winter (December–February, DJF, mean) and (b) boreal summer (June–August, JJA, mean) in Euro-Mediterranean Centre on Climate Change coupled climate model (CMCC-CM2) climatology. (c and d) Differences with CRU data set.

areas, while temperature bias remains negative in northern high latitudes and turns into positive in tropical and midlatitude continents in the boreal summer (Figure 2). The negative bias in the Northern Hemisphere high latitudes in summer is consistent with an overestimation of the Canadian and Siberian snow extents (not shown). ERA-Interim over land is in good agreement with CRU data set, even though the latter is slightly warmer in the Northern Hemisphere (Jones et al., 2012). Globally, the coupled model land temperature (excluding Antarctica as not present in the CRU data set grid) is about 12.7 °C, while in ERA-Interim and CRU it is about 13.2 °C and 13.5 °C, respectively (Table 1).

In the Northern Hemisphere high latitudes (60–90°N), the seasonal cycle of the temperature at 2 m over land confirms the presence of a cold bias that is larger in the core of the boreal winter and summer seasons (Figure 3a). Cold biases affecting the entire annual cycle are also noticeable in West Africa (20°W to 40°E, 5–30°N; Figure 3h) and South Asia (70–110°E, 5–25°N; Figure 3f). Over North Europe (10°W to 50°E, 40–70°N) and North America (170–60°W, 45–70°N) the seasonal cycle of the 2 m temperatures is realistic in intensity and time evolution (Figures 3b and 3d). The Mediterranean (10°W to 50°E, 30–45°N) summer and the second part of the year (August–November) in South America/Amazon (70–55°W, 30°S to the equator) show higher temperature in the model than in reanalysis (Figures 3c and 3e).

Global annual mean precipitation in CMCC-CM2 is about 3.3 mm/day, larger than the value computed from GPCP (i.e., 2.7 mm/day; see Table 1). The largest precipitation deviations are located in the tropical sector (Figure 4), with the annual zonal mean overestimated at all latitudes (Figure 4a). The major discrepancies are noticeable in middle-to-high latitudes (60°N and 60°S) and in the tropics. Here, in particular, the peak in the Southern Hemisphere exceeds the GPCP mean precipitation by almost 2 mm/day, the one in the Northern Hemisphere is overestimated by about 1 mm/day. The location of the maximum of precipitation over all longitudes is identified as the position of the Intertropical Convergence Zone (ITCZ; Marshall et al.,

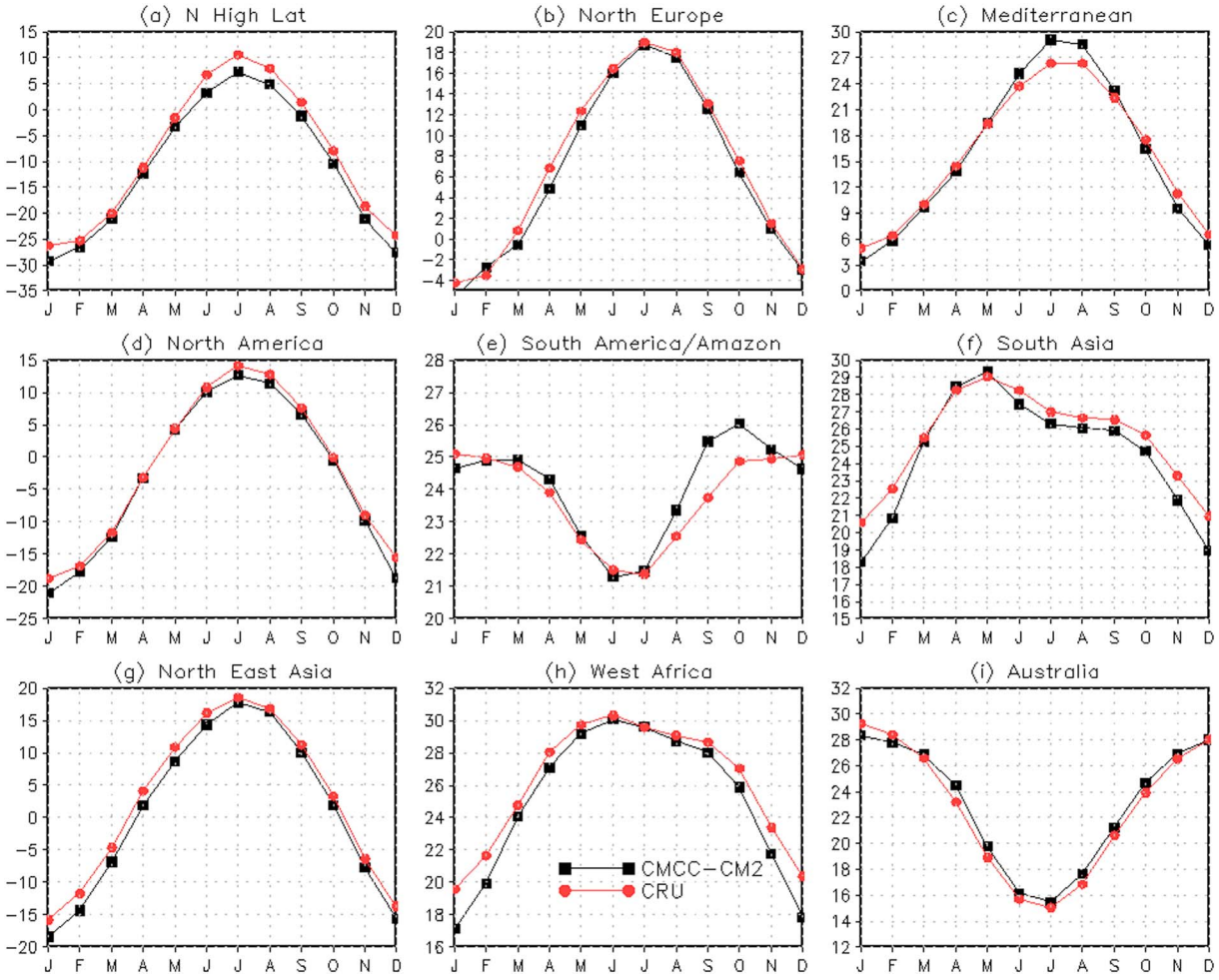

Figure 3. Annual cycle of temperature (°C) at 2 m averaged over selected regions for the Euro-Mediterranean Centre on Climate Change coupled climate model (CMCC-CM2) climatology (black line) and for CRU (red line) data set. The regions are (a) northern high latitudes (60–90°N), (b) northern Europe (10°W to 50°E, 40–70°N), (c) Mediterranean region (10°W to 50°E, 30–45°N), (d) North America (170–60°W, 45–70°N), (e) South America/Amazon (70–55°W, 30°S to the equator), (f) South Asia (70–110°E, 5–25°N), (g) Northeast Asia (80–130°E, 30–60°N), (h) West Africa (20°W to 40°E, 5–30°N), and (i) Australia (115–140°E, 40–15°S).

2014) that corresponds to about 6°N for both GPCP and CMCC-CM2 (Table 1). In the model the maximum of zonally averaged precipitation extends up to 9°N, but simulated values still peak at 6°N.

In boreal winter, the model shows dry biases in the equatorial Pacific Ocean, in the western Atlantic Ocean just north of the equator and in the Amazon basin, while wet biases are spread out in the Indo-Pacific region off the equator and in the southern tropical Atlantic Ocean (Figure 4c). Excess of precipitation are also present in the middle-to-high latitudes sector of both the main oceans (Figure 4c).

In boreal summer, rainfall is overestimated in the Indian Ocean, while a lack of summer monsoon precipitation is noticeable over India and most of coastal Southeast Asia (Figure 4e). In the next section this bias will be analyzed in depth considering implications in terms of model performance in reproducing monsoons. The wet wintertime bias in northern Pacific Ocean disappears in the summer, but the overestimated rainfall in the tropics extends northward and southward (Figure 4e). Compared to winter, the equatorial Atlantic Ocean and the Amazon biases are reduced, although still present (Figure 4e). In particular, the underestimation of precipitation over the Amazon region is due to a combination of factors, including biases in the large-scale circulation and feedbacks between moisture transport and the Pacific and Atlantic SSTs (Martins et al., 2015). Also, the diurnal cycle of precipitation in the region is not-well resolved in CAM5.3, with precipitation peak tied too closely to the solar insolation (Bogenschutz et al., 2018). Improvements in the timing of the diurnal cycle in more recent model versions does not necessarily imply better simulated

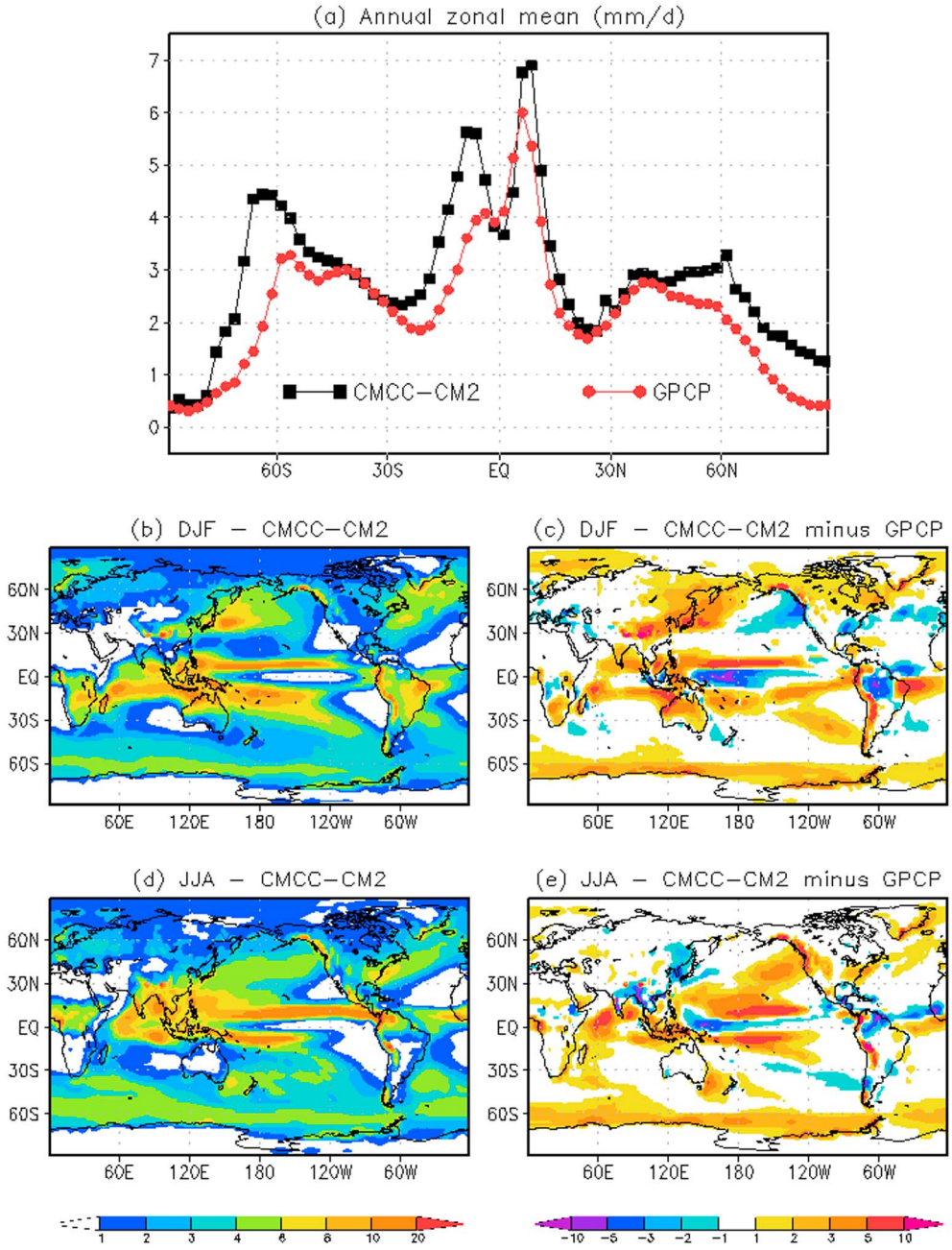

Figure 4. (a) Annual zonal mean precipitation (mm/day) for CMCC-CM2 (black line) and Global Precipitation Climatology Project (GPCP; Adler et al., 2003) data (red line). Maps of (b) December–February (DJF) and (d) June–August (JJA) mean precipitation (mm/day) for CMCC-CM2 and (c, e) differences with GPCP. CMCC-CM2 = Euro-Mediterranean Centre on Climate Change coupled climate model.

precipitation intensity in the region (Bogenschutz et al., 2018). The dry bias over the Amazon catchment, combined with the bug in the fire module was mostly responsible for an excessive fire ignition in the region, and then corrected (Li et al., 2014).

Overestimation of precipitation in the eastern Pacific Ocean is symptomatic of the well-known double ITCZ issue exhibited in most of state of the art coupled climate models (Bellucci et al., 2010; Hwang & Frierson, 2013; Mechoso et al., 1995). In CMCC-CM2 the annual mean precipitation averaged in the eastern Pacific (the area 20°S to the equator, 100–150°W) is about 3.91 mm/day, indicative of a moderate to high bias if compared with the values shown in Bellucci et al. (2010).

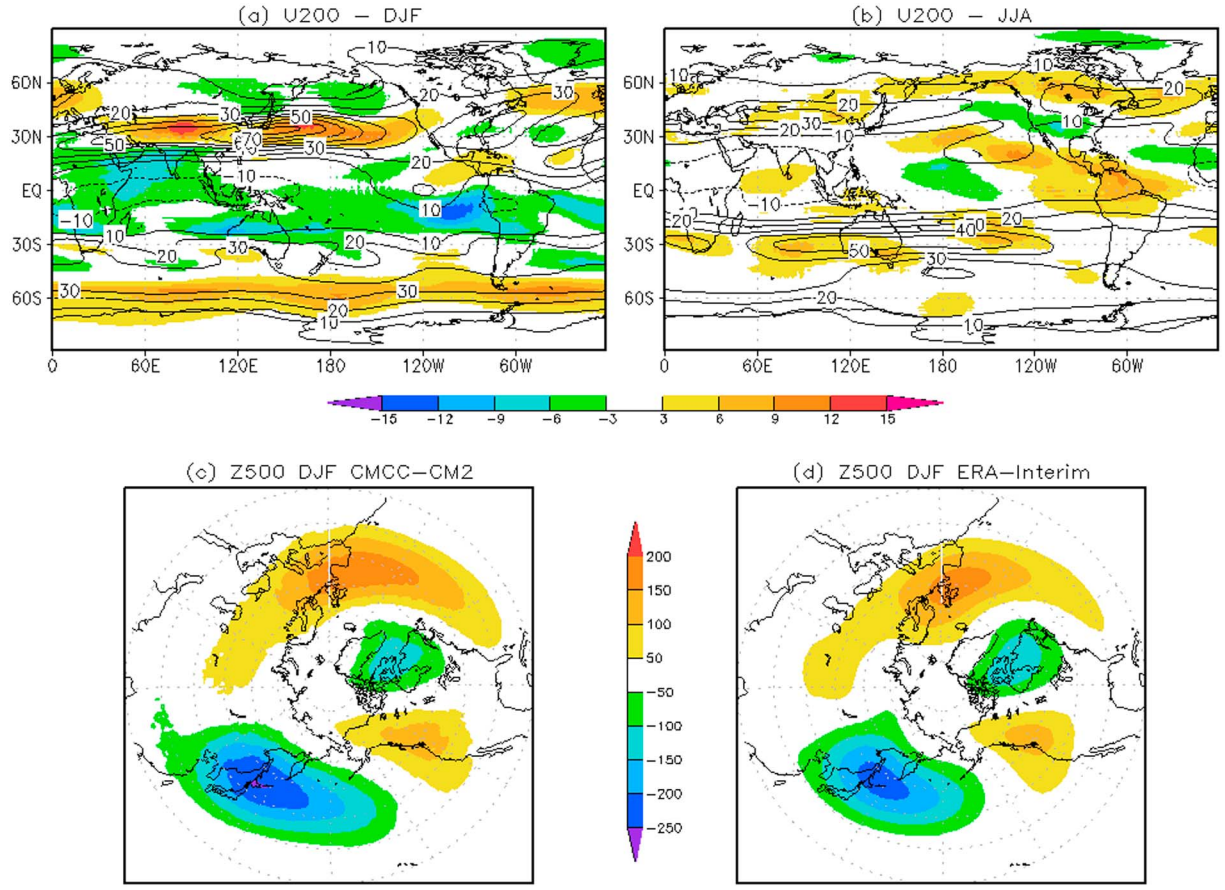

Figure 5. (a) December–February (DJF) and (b) June–August (JJA) means zonal wind (m/s) at 200 hPa in terms of CMCC-CM2 climatology (contours) and as differences (shaded) with ERA-interim data. (c,d) Eddies (i.e., departures from zonal mean) of geopotential height (m) at 500 hPa in DJF for CMCC-CM2 and ERA-Interim data, respectively. CMCC-CM2 = Euro-Mediterranean Centre on Climate Change coupled climate model.

The upper troposphere summer jet is realistically reproduced with small positive differences in the western Atlantic (Figure 5b), while the winter westerlies over Asia/western Pacific are overestimated as well as the tropical easterly jet (Figure 5a). Common model deficiencies include an equatorward bias in the location of the midlatitude westerlies and an overly zonal orientation of the North Atlantic storm track (Shepherd, 2014). Compared with CMIP5 state of the art models, the Atlantic winter bias structure is in line with other models but intensities are weaker (Zappa et al., 2013). In summer the bias is mostly located over the Atlantic where the model jet is stronger than observed, differently from CMIP5 models ensemble mean bias (Zappa et al., 2013). Recent findings suggest that improved parameterization of low-level drag may alleviate typical circulation biases in coarse-resolution climate models (Pithan et al., 2016).

In Figures 5c and 5d, the stationary wave pattern is represented in terms of maps of the departures from the zonal mean of the geopotential height field at 500 hPa for the Northern Hemisphere winter (December–February, DJF, mean). In the midtroposphere the boreal winter eddies regime is well captured (Figures 5c and 5d), with a pattern correlation of 0.95 between CMCC-CM2 and ERA-Interim. In fact, the position of the ridges and troughs is realistic, including the position of maxima and minima over western Northern Europe and western North America, and over northwestern Pacific boundaries and Alaska, respectively. The intensities are also realistic, with the troughs more intense than in the reanalysis (Figures 5c and 5d). Current knowledge and sensitivity experiments suggest that we have less confidence in the atmospheric circulation aspects of climate change, primarily controlled by dynamics and able to exert a strong control on regional climate (Shepherd, 2014).

SST patterns are well represented in CMCC-CM2 (Figure 6). In terms of annual mean, regions where the systematic SST error exceeds 1 °C are limited and mostly localized in the Northern Hemisphere (Figures 6a and

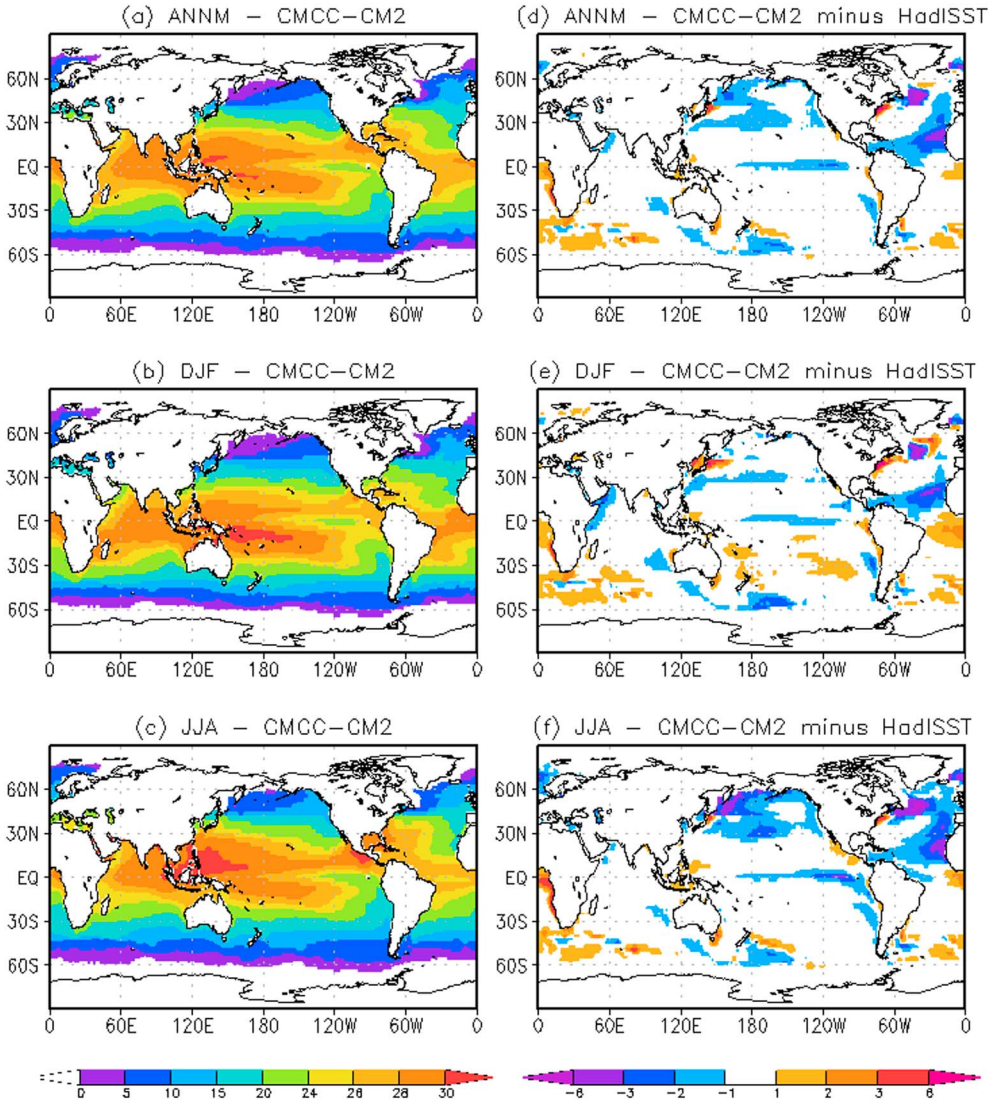

Figure 6. (a) Annual, (b) December–February (DJF), and (c) June–August (JJA) mean sea surface temperature for Euro-Mediterranean Centre on Climate Change coupled climate model (CMCC-CM2) and (d–f) differences with HadISST (Rayner et al., 2003).

6d). The common warm SST bias, affecting the ocean eastern boundaries in the large majority of global climate models (Large & Danabasoglu, 2006; Richter, 2015), is very narrow along the coasts of California and west South America, while it is still remarkable in southeastern tropical Atlantic, along the Angola and Benguela coasts.

The cold bias found in the North Atlantic at about 45°N (Figures 6d–6f) is also common to many coupled models (Wang et al., 2014) and is a typical feature of NEMO ocean model, mostly at 1° horizontal resolution, in forced mode as well (Danabasoglu et al., 2014). A possible explanation for this systematic error is the relative low horizontal resolution of state of the art global coupled model and associated representation of the Gulf Stream and North Atlantic current paths (Hewitt et al., 2016; Iovino et al., 2016). In summer, the anomalies in the Atlantic Ocean intensify with respect to the winter, and large cold anomalies are seen also in the North Pacific Ocean (Figure 6f). Summer cold anomalies are more intense and extensive off the African coasts of the tropical North Atlantic. This is likely associated with the dust emissions from the Sahara desert, which shields the shortwave radiation at the sea surface (Albani et al., 2014). Recent findings assessed that dust found in the atmosphere is substantially coarser than represented in current global climate models

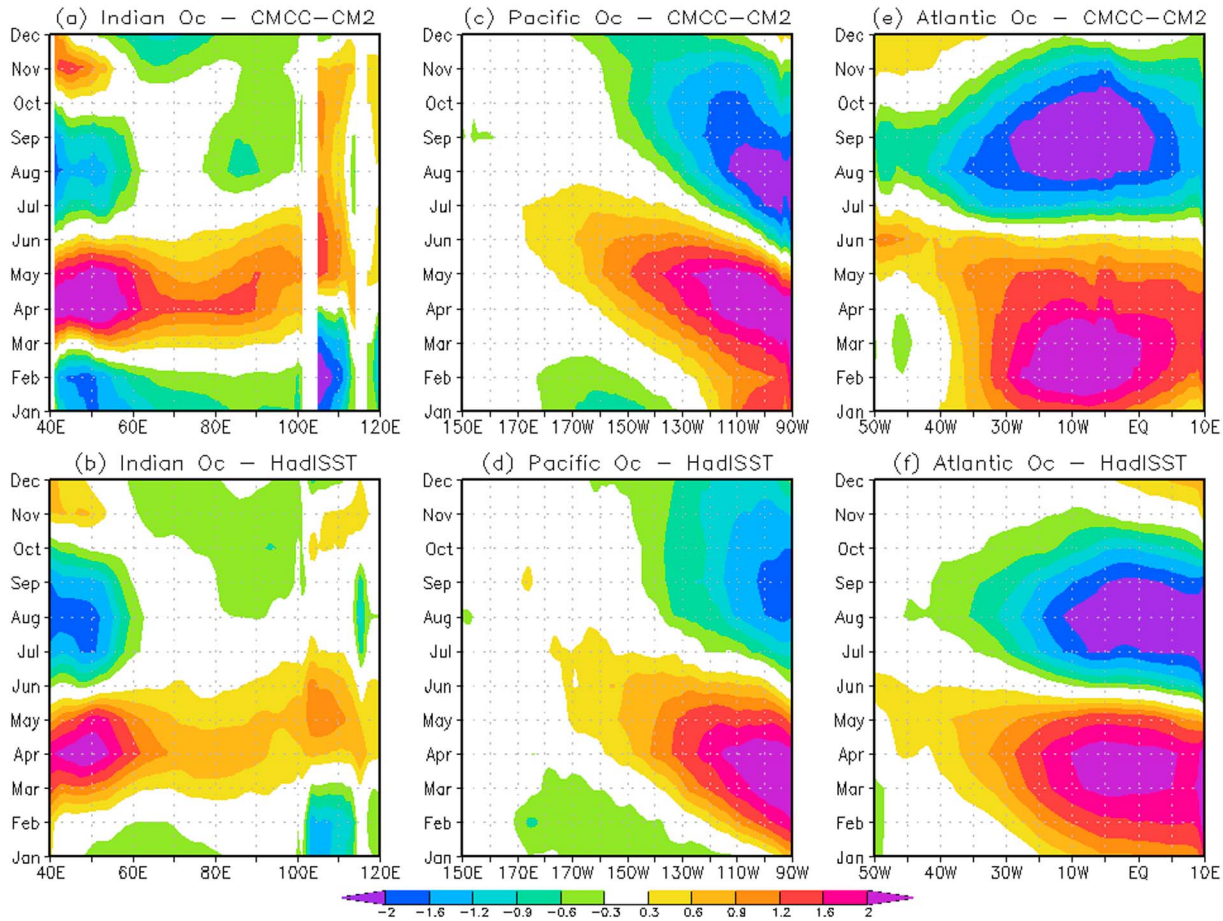

Figure 7. Seasonal variation (relative to its annual mean) of SST (°C) averaged at the equator (5°S to 5°N) in (a, b) Indian Ocean, (c, d) Pacific Ocean, and (e, f) Atlantic Ocean for Euro-Mediterranean Centre on Climate Change coupled climate model (CMCC-CM2) and the HadISST data set, respectively.

(Kok et al., 2017). Hence, the lightweight dust represented by CMCC-CM2 could be more erratic during simulated dust storms and spreads out over the Atlantic contributing to the cold SST bias. SST positive and negative biases tend to compensate in the spatial average that results to be 20.3 °C in the model and 20.5 °C in the HadISST annual climatology (Table 1). As already specified, this SST values are computed without taking into account the value of SST below sea ice, to have a clean comparison between model and HadISST data set.

Compared to the previous version of the CMCC coupled model, the SST biases are largely reduced in the Southern Hemisphere and show smaller extension, but opposite sign, in the equatorial Pacific. Instead, the large negative biases in the North Pacific and North Atlantic remain (see Scoccimarro et al., 2011). The improvements described for the CMCC coupled model are satisfactory but their specific causal attribution is made difficult by the radical differences between the present configuration and the previous one. A similar experiment performed with the CESM climate model (Small et al., 2014), mostly differing from CMCC-CM2 for the oceanic component, allows an indirect comparison, revealing as well some improvements in the SST over the Indian and Pacific Oceans. Specifically, in CMCC-CM2 the cooling in the Indian Ocean is largely reduced. In the tropical Pacific Ocean the warm bias in the east in the CESM model is replaced by a small (not exceeding 1 °C) cold bias along the equator. In the Southern Hemisphere the cold bias is replaced by a warm one. In the North Pacific Ocean the biases in CMCC-CM2 are of the same sign as in CESM but with a reduced intensity. Instead, in the Atlantic Ocean the structure and intensity of the biases is comparable in the two models.

Important aspects of the equatorial dynamics and related large-scale phenomena are associated with the annual cycle of SST (Figure 7). The annual cycle in the eastern equatorial Pacific can serve as indicator of the performance of CGCMs as it involves complex dynamical and physical interactions among climate

subsystems (Song et al., 2014). CMCC-CM2 simulates a realistic annual cycle variation of SST in the equatorial Pacific Ocean (average between 5°S and 5°N) with the warm March–April phase and the cold August–October phase (Mitchell & Wallace, 1992; Nigam & Chao, 1996) well reproduced except for the negative anomalies being more intense and the warm anomalies extending farther west (Figures 7c and 7d). Coupled ocean-atmosphere processes, like wind-evaporation-SST feedback, stratus-SST feedback and upwelling-SST feedback, are responsible for the annual character of the dynamics in the eastern equatorial Pacific (Xie, 2004, for a review). In both CMCC-CM2 and HadISST, the seasonal cycle of SST along the equator in the Pacific Ocean has a westward propagation that is related to the seasonal cycle of wind stress, coupled ocean-atmosphere processes, and ocean dynamics (i.e., Chang, 1994; Dijkstra & Neelin, 1995; Yu & McPhaden, 1999).

The annual cycle of equatorial SST in the Atlantic Ocean is characterized by a transition from the warm pool in March–May to the development of the cold tongue in the east in June–August (JJA; Figure 7f). The Atlantic cold tongue seasonality is largely associated to wind driven upwelling (Philander & Pacanowski, 1981; Wang, Jin, Wu, & Hsu, 2017). The timing of this transition is correctly simulated, but the summer cold anomaly is not realistically confined east of the basin, rather its maximum is mostly located toward the central Atlantic (Figure 7e). This characteristic is common to other CMIP5 models, where the annual cycle of the upwelling tends to be systematically too strong (Wang, Jin, & Wu, 2017).

The annual cycle of equatorial SST in the Indian Ocean is mostly characterized by warm anomalies in the western sector between March and May, before the monsoon season, and by cold anomalies thereafter, in correspondence of the onset and establishment of the South Asian summer monsoon (Figure 7b). An important difference with the other basins is that the area with largest anomalies corresponds to the western part of the basin, where the interaction with the seasonal march of the monsoon winds is very strong (Schott & McCreary, 2001). In CMCC-CM2, the warm phase is stronger than observed while the cold one is weaker (Figure 7a). The misrepresentation of east west SST gradient along the equator in the pre-monsoon season and related surface wind biases are common to CMIP5 models, which may lead to a wrong simulated monsoon climatology (Annamalai et al., 2017).

Other important characteristics of the oceanic component frequently used to evaluate the model performance are transports of heat and mass, here characterized in terms of their patterns and relative strengths (Figure 8). In CMCC-CM2 the maximum northward global ocean mean heat transport is about 1.79 PW at 15°N (Figure 8a and Table 1), consistent with the 1.7 ± 0.3 PW maximum estimated by Trenberth and Fasullo (2008) at the same latitude (shown in Figure 8a by a black circle with its error bar). The maximum southward transport of 0.87 PW in the model agrees with the estimated value of 1.2 ± 0.5 PW (Trenberth & Fasullo, 2008) but it is located at 13°S instead of 11°S (the observed estimated value is shown in Figure 8a by a black circle with its error bar). In general, both the latitudinal pattern and the values of the global Meridional Heat Transport match with the estimates given by a set of eddy-permitting global ocean reanalyses (Masina et al., 2017). A large portion of the global northward mean transport is provided by the Atlantic Ocean: in CMCC-CM2 the value of the time-mean Atlantic Meridional Heat Transport at 26.5°N is 1.08 PW, slightly weaker than the estimate of 1.31 ± 0.40 as given by first years measurements (Johns et al., 2011) provided by the RAPID/MOCHA program (Cunningham et al., 2007). More recent values evidenced a decrease with a drop up to 1.14 ± 0.08 for the pentad 2009–2013 (McCarthy et al., 2015).

Ocean mass transport is represented in terms of meridional overturning circulation (MOC). The MOC is shown in Figures 8b and 8c as zonally averaged annual mean meridional overturning stream function for the globe and the Atlantic basin, respectively. The global MOC shows the upper-ocean northward flow ultimately reaching the North Atlantic subpolar gyre, the effect of winds at the surface and the sinking of waters formed in the north that move back toward the Southern Ocean (Figure 8b). There the Deacon cell peaks to 25 Sv in the upper 1,000-m depth around 50°S (Figure 8b). As for the heat, most of the mass transport in the Northern Hemisphere is provided by the Atlantic Ocean (Figure 8c). In CMCC-CM2, the Atlantic MOC presents the two overturning cells linked to the formation of North Atlantic Deep Water and Antarctic Bottom Water. The North Atlantic Deep Water consists of northward surface flow in the upper 1000 m, sinking north of 50° and a southward return flow between 1,000- and 3,000-m depths. It reaches its maximum strength of ~24 Sv at a depth of 1,000 m around 40°N. The Antarctic Bottom Water cell fills the deep ocean

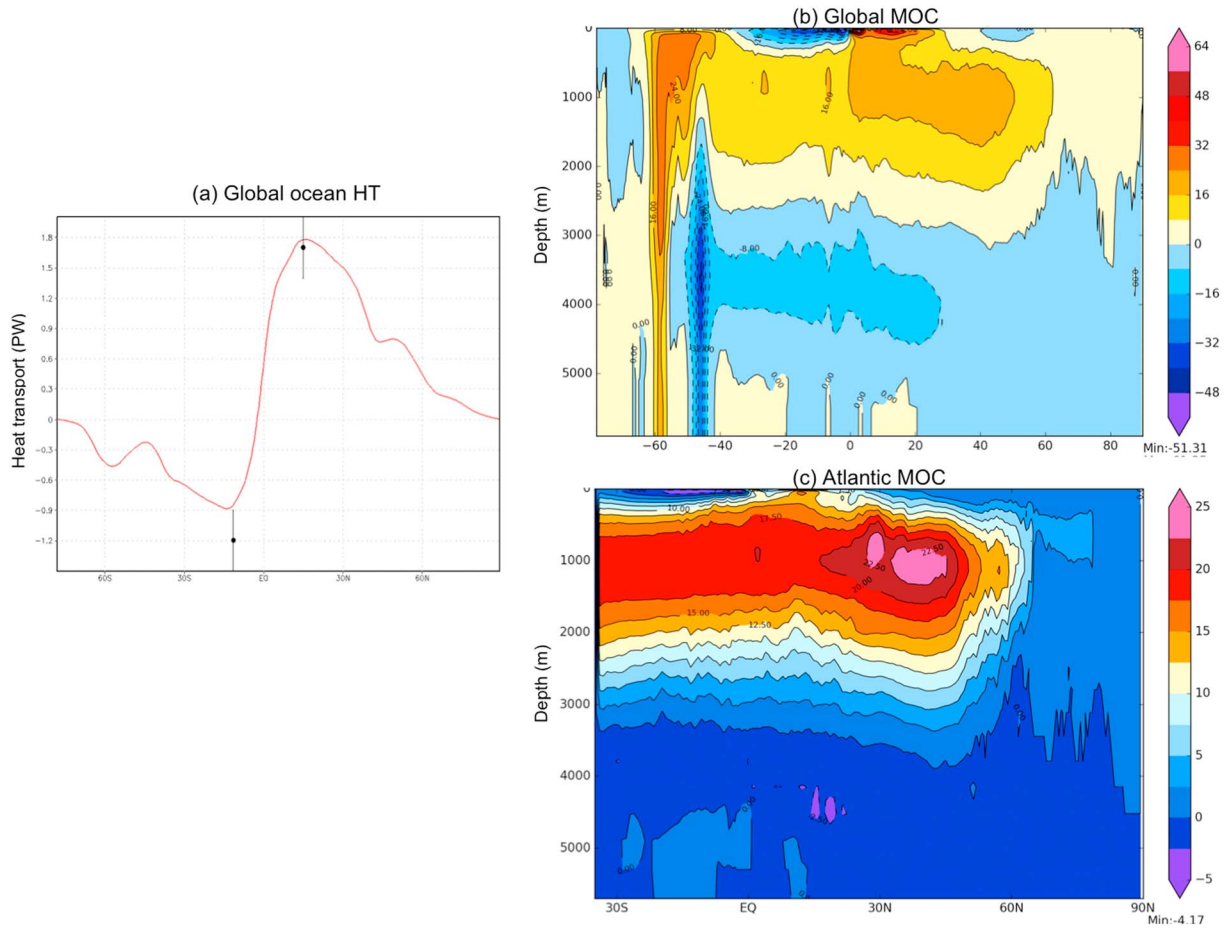

Figure 8. (a) Global ocean annual mean heat transport (PW) for CMCC-CM2 (red line) and estimated values (black circle with error bars) as in Trenberth and Fasullo (2008). (b) Global and (c) Atlantic annual mean meridional overturning circulation (MOC, Sv) for CMCC-CM2 (contours are 8 and 2.5 Sv, respectively). CMCC-CM2 = Euro-Mediterranean Centre on Climate Change coupled climate model.

below 3,000 m and reaches ~6 Sv. The cross-equatorial transport is ~18 Sv. The mean value of the AMOC at 26.5°N in the model is 19.4 ± 2.3 Sv (Table 1). The value is close to the upper bound of the RAPID/MOCHA estimate of 17.0 ± 3.6 Sv for the period 2004–2013 (McCarthy et al., 2015) and stronger than the ensemble mean value of 15.61 ± 2.8 Sv from an ensemble of eddy-permitting global ocean reanalyses (Masina et al., 2017).

Figures 9a and 9b shows the annual cycle of the sea ice extent in the Northern and Southern Hemispheres. The model (red line) tends to underestimate the mean extent in the Northern Hemisphere during boreal summer and for the whole year in the Southern Hemisphere if compared with NSIDC estimates (black line). Other panels show the simulated climatology of the sea ice concentration in boreal summer (July–September, JAS) and boreal winter (January–March, JFM) for both hemispheres. The simulated Arctic sea ice concentration has a maximum over 95% during boreal winter reducing to about 40% during boreal summer (Figures 9c and 9e). However, the sea ice concentration in the Arctic is underestimated during boreal summer with values exceeding 15% (blue color in Figure 9e) confined within the black thick line that is the NSIDC estimated sea ice extent (defined by the area exceeding 15% of sea ice concentration). In the Southern Hemisphere the sea ice edge is realistically captured in austral summer (Figure 9d), as the NSIDC estimated sea ice extent likely corresponds to the blue color shaded values (indicating sea ice concentrations larger than 15%), while it is slightly underestimated in austral winter (Figure 9e). The ability of CMCC-CM2 to realistically simulate the present climate sea ice extent is a good starting point for the estimation of the polar climate sensitivity to external forcing and perturbed initial conditions in climate projections or in seasonal forecasts of sea ice extent (Hall & Qu, 2006).

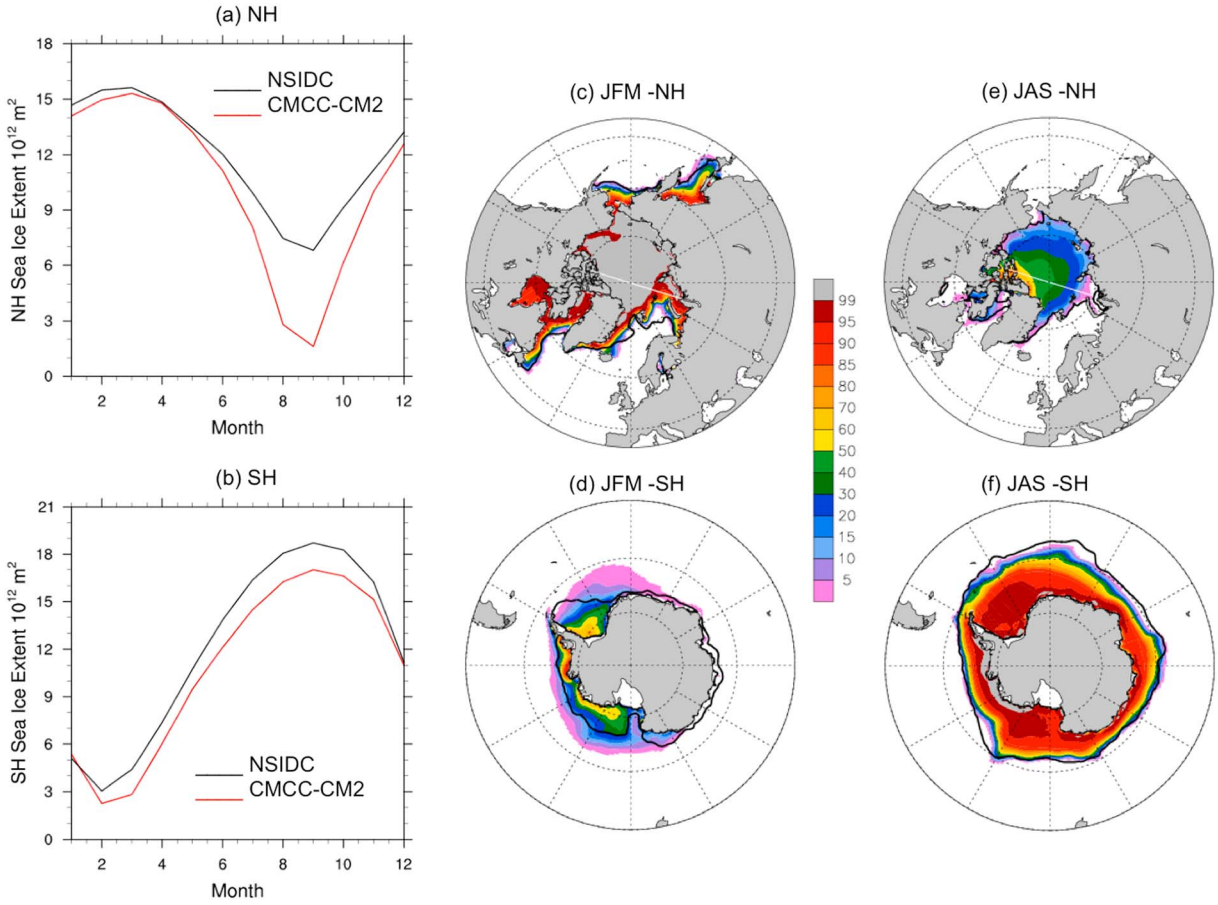

Figure 9. Annual cycle of sea ice extent (10^6 km^2) in (a) the Northern Hemisphere and (b) the Southern Hemisphere for CMCC-CM2 (red line) and NSIDC estimates (black line). JFM and JAS mean sea ice concentration (%) in (c, e) the Northern Hemisphere and (d, f) the Southern Hemisphere projections. The solid black line in panels c–f indicates the estimated NSIDC value corresponding to the limit of the observed sea ice extent (computed as the area with sea ice concentration larger than 15%). CMCC-CM2 = Euro-Mediterranean Centre on Climate Change coupled climate model; NSIDC = National Snow and Ice Data Center; JFM = January–March; JAS = July–September.

4. Main Patterns of Variability

4.1. Middle-To-High Latitudes Winter Main Teleconnection Patterns

The dominant modes of variability and associated teleconnection patterns are usually identified in terms of empirical orthogonal functions (EOFs) of specific variables. Figure 10 shows the first two EOFs of boreal winter (DJF) mean sea level pressure for the Northern Hemisphere (20–90°N). The first EOF explains more than 30% (Figure 10c) of the Northern Hemisphere variability in winter and is identified as Northern Annular Mode (NAM; Thompson & Wallace, 2000). The pattern is clearly dominated by the NAO (North Atlantic Oscillation; Walker & Bliss, 1932; van Loon & Rogers, 1978; Hurrell, 1995) structure in the Atlantic sector, with positive anomalies over the Pacific sector yielding a more annular structure (Figure 10c). The NAO is characterized by a redistribution of atmospheric mass between the Arctic and the subtropical Atlantic, and it is the leading mode of the North Atlantic sector largely affecting Europe (Hurrell et al., 2003). Seasonal forecasts of the winter NAO are now starting to show valuable skill (Athanasiadis et al., 2017; Scaife et al., 2014); hence, an accurate simulation of the NAO in a state of the art climate coupled model is a particularly valuable feature.

The model is able to realistically represent the NAM main pattern of variability (Figure 10a). In fact the explained variance for the first EOF is 31.4%, in line with the value obtained from ERA-Interim. Also, the pattern correlation (i.e., spatial correlation of EOF1 in the model and in ERA-Interim) is 0.82. The spatial correlation is high, indicative of a good correspondence between the two patterns, even though, compared to the

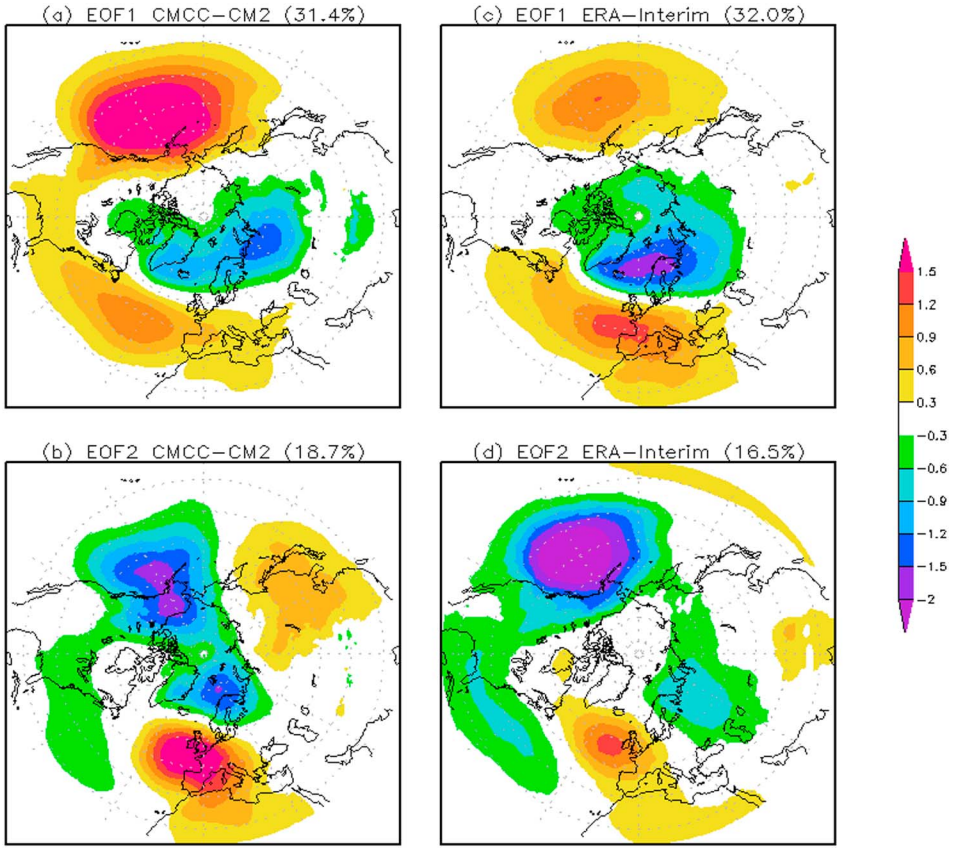

Figure 10. EOF1 and EOF2 of December–February SLP anomalies (mb) in the Northern Hemisphere (20–90°N) for (a, b) CMCC-CM2 and (c, d) ERA-Interim. CMCC-CM2 = Euro-Mediterranean Centre on Climate Change coupled climate model; EOF = empirical orthogonal function.

reanalysis, the North Pacific positive anomaly is overly strong, while the negative center of action of the model NAO dipole displays an eastward shift toward Siberia (Figures 10a and 10c). The second EOF explains about 16% of the variance in ERA-Interim (Figure 10d) and has a primary center of action in the vicinity of the climatological mean Aleutian low (Smoliak & Wallace, 2015). The model consistently reproduces the observed variance associated with this mode (around 19%) but the spatial pattern correlation is weaker (0.7) than for EOF1.

The EOF2 of boreal winter sea level pressure (SLP) in the Northern Hemisphere is also addressed as surface signature (Smoliak & Wallace, 2015) of the Pacific North American (PNA) pattern, one of the most prominent modes of low-frequency variability in the Northern Hemisphere extratropics (Barnston & Livezey, 1987). The PNA is visible in all months, except for June and July, with the largest spatial scale observed during boreal winter. The relative pattern exhibits a quadrupole structure in 500-hPa height anomalies, with centers of equal polarity located south of the Aleutian Islands and over the southeastern United States and centers of opposite sign located in the vicinity of Hawaii, and over the intermountain region of North America (Barnston & Livezey, 1987). In the ERA-Interim reanalysis, the PNA appears as the EOF2 of geopotential height anomalies at 500 hPa in winter (DJF mean), explaining around 17% of the total variance (Figure 11d), while in the model it is the dominant mode of variability of the Northern Hemisphere winter 500-hPa geopotential height, explaining around 30% of the variance (Figure 11a). It is worth noticing that in ERA-Interim the two leading EOFs of 500-hPa geopotential height explain a comparable fraction of variance (23.1% and 16.5%, respectively; Figures 11c and 11d).

The Southern Annular Mode (SAM) describes the north-south movement of the westerly wind belt that circles Antarctica, dominating the middle to higher latitudes of the Southern Hemisphere (Rogers & van Loon, 1982). The changing position of the westerly wind belt influences the strength and position of cold fronts and

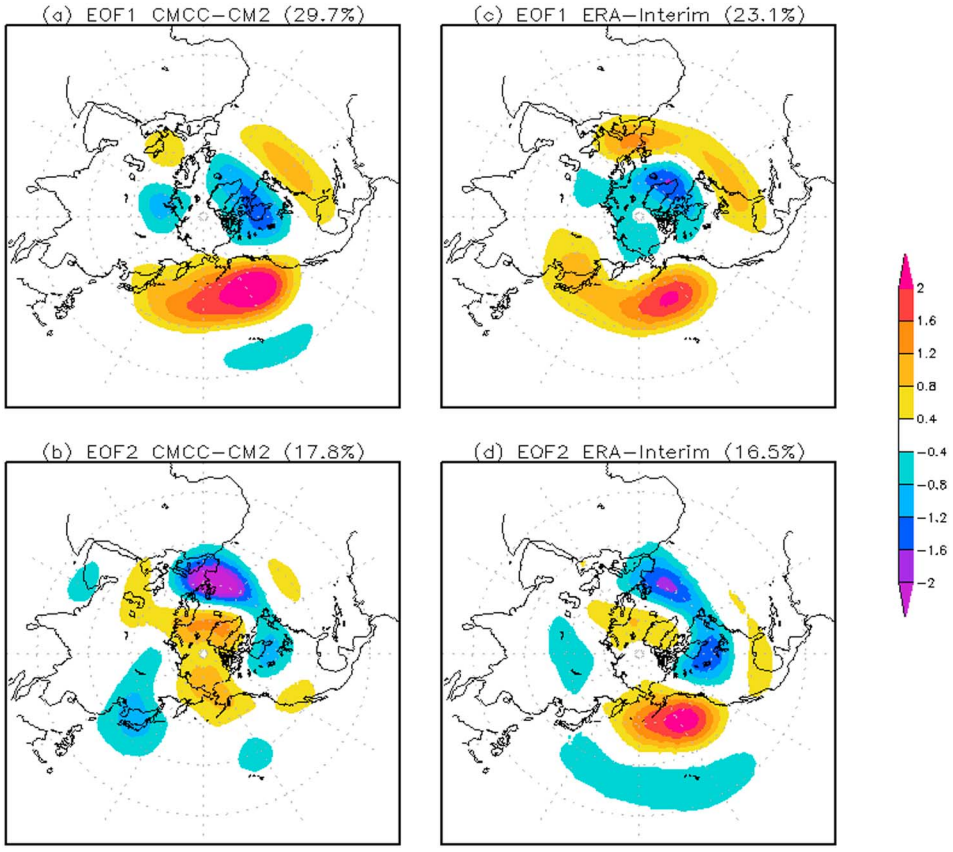

Figure 11. (a, c) EOF1 and (b, d) EOF2 of December–February geopotential height at 500-hPa anomalies (m) in the Northern Hemisphere (equator to 90°N) for CMCC-CM2 (EOF1) and ERA-Interim (EOF2), respectively. CMCC-CM2 = Euro-Mediterranean Centre on Climate Change coupled climate model; EOF = empirical orthogonal function.

midlatitude storm systems, and it is an important driver of rainfall variability in southern Australia (Hendon et al., 2007). The SAM pattern can be identified in terms of empirical orthogonal functions of SLP anomalies (Rogers & van Loon, 1982). In austral winter (JAS) the SAM is the leading mode of SLP variability, explaining about 30% of the variability (Figure 12). This pattern is realistically reproduced by the model with a spatial correlation of 0.78. In recent years, a high positive SAM has dominated the austral autumn–winter variability, and has been a significant contributor to the "big dry" observed in southern Australia from 1997 to 2010 (Ummenhofer et al., 2011).

4.2. Tropical Variability: ENSO, IOD, and Monsoons

The variability in the tropical region is mostly dominated by ENSO (El Niño–Southern Oscillation) and its teleconnections. As previously described (section 3) the seasonal evolution of SST and winds along the equatorial Pacific is crucial for the ENSO dynamics. In terms of variability, a good measure of ENSO variability in time is given by SST indices in specific regions. One of the most common ENSO indices is NINO3.4 that corresponds to the SST anomalies averaged in the Nino3.4 region (170–120°W, 5°S to 5°N). Figure 13a shows the Power Spectrum Density of the NINO3.4 index for CMCC-CM2 and observations. For the model the spectrum is applied to the NINO3.4 index computed for the last 100 years of the experiment considered, while in the observations we considered the SST for the whole twentieth century taken from HadISST data set (Rayner et al., 2003). In terms of frequency the model is able to reproduce the observed around 4–5 years spectral peak, but the amplitude is larger than observed. The patterns of the ENSO teleconnections are represented in Figures 13b–13e in terms of linear regression (Langenbrunner & Neelin, 2013) between NINO3.4 and precipitation (shaded) and sea level pressure (contours) averaged in boreal winter and boreal summer, respectively. The precipitation anomalies associated with ENSO are realistically represented in summer (Figures 13d and 13e) when the double ITCZ bias affecting the Tropical Pacific is less evident with a consistent

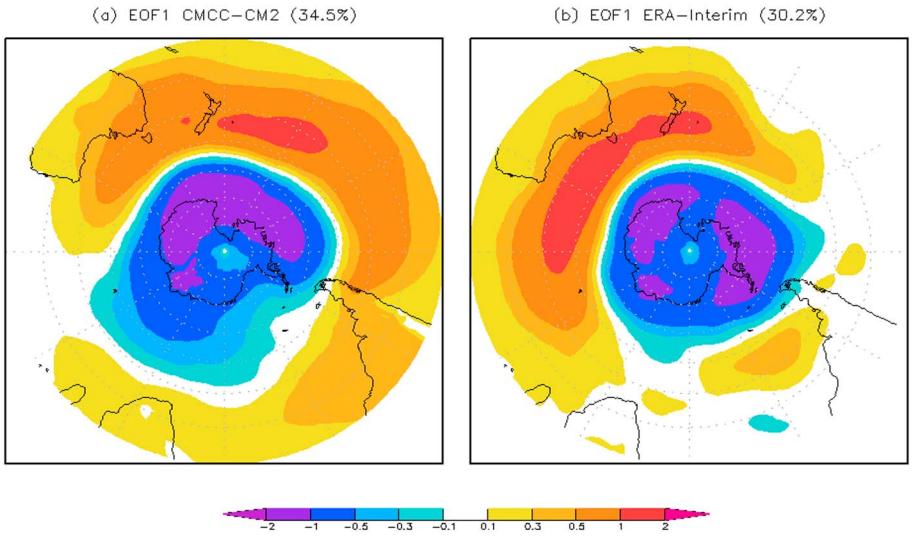

Figure 12. EOF1 of July–September SLP anomalies (hPa) in the Southern Hemisphere (90–20°S) for (a) CMCC-CM2 and (b) ERA-Interim. CMCC-CM2 = Euro-Mediterranean Centre on Climate Change coupled climate model; EOF = empirical orthogonal function.

representation of the ENSO-rainfall covariance over India, the Maritime Continent and the tropical Atlantic. On the other hand, winter season is heavily affected by the double ITCZ feature in the model, which in turn affects the shape of the ENSO-precipitation covariance structure (Figures 13b and 13c). For the SLP anomalies, the patterns are better represented in JFM than in JJA (mostly in the Northern Hemisphere), apart from the anomalies in the western Pacific (Figures 13b and 13c). In boreal summer the SLP anomalies in the Southern Hemisphere are poorly reproduced, possibly affecting the model performance of the Pacific South American pattern (Mo & Paegle, 2001).

The ENSO variability and its impact on precipitation over India is known to be influenced by the Indian Ocean Dipole (IOD, Saji et al., 1999), a temperature dipole between the eastern and western sector of the Indian Ocean developing during the monsoon and peaking in boreal fall. Despite peaking after the monsoon demise, its developing phase can have large impact on the monsoon and modulate the effect of ENSO on the monsoon itself, tuning the interaction between Walker circulation and local Hadley cell in the Indo-Pacific sector (Ashok et al., 2001). The IODM (IOD Mode), computed as the difference in SST anomalies between the tropical western Indian Ocean (50–70°E, 10°S to 10°N) and the tropical southeastern Indian Ocean (90–110°E, 10°S to the equator; Saji et al., 1999), is the index to measure the IOD variability. Figure 14 shows the linear regression of precipitation and lower tropospheric winds averaged during OND, the season where the dipole peaks, on the IODM index. The typical precipitation and wind pattern associated with the IOD is characterized by a dipole in the precipitation between the western and eastern side of the basin, mimicking the peak in the SST field and intense easterlies along the equator (Figure 14b). This feature is realistically reproduced in the model (Figure 14a), but with weaker intensity. East of 90°E, the modeled Indian Ocean is biased with positive precipitation anomalies (Figure 14a). The Eastern African short rains, defined as second and smaller peak of seasonal rainfall in the region (Hastenrath et al., 1993) and related with the IOD pattern (Behera et al., 2005), are underestimated with respect to the observation, despite the improved IOD aspects.

Another important aspect of variability in the tropics is related with the monsoons that drive the global hydrological cycle. Wang and Ding (2008) introduced the concept of a global monsoon with specific metrics. The intensity and spatial extent of the global monsoon can be identified in terms of seasonal difference of precipitation, that is, JJA minus DJF, as shown in Figure 15 for the model and GPCP data set. The area shown in Figure 15 and enclosed in the tropical band is identified as the global monsoon area (Hsu et al., 2013). With respect to observations, CMCC-CM2 shows larger precipitation seasonal differences over the central tropical Pacific Ocean in both hemispheres (Figure 15a). Over land, Northern Hemisphere precipitation peaks and Southern Hemisphere minima represent the main monsoon regions. In particular, the maxima in the

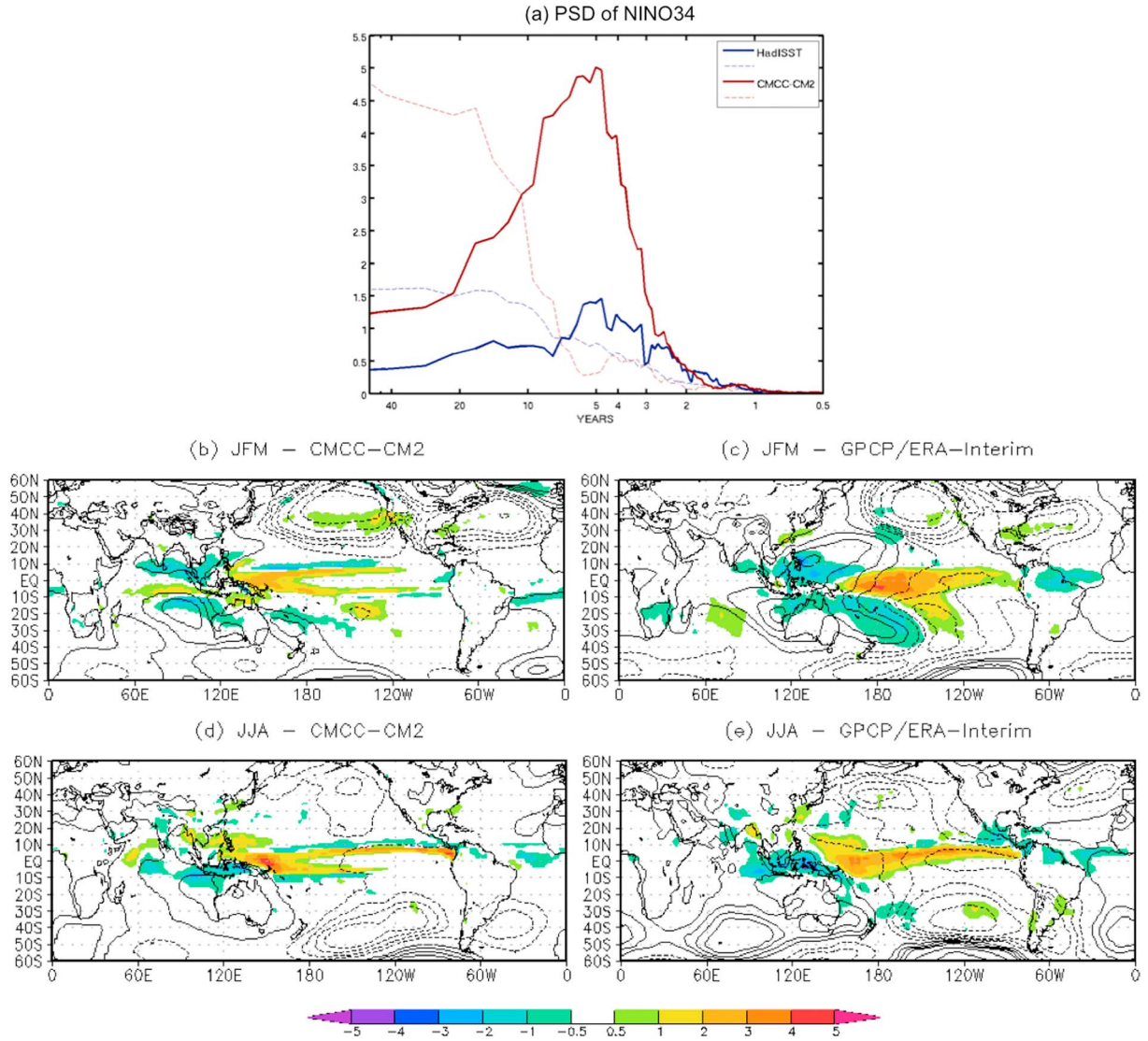

Figure 13. (a) PSD of NINO3.4 index for HadISST (blue line) and CMCC-CM2 (red line). The PSD is computed by means of the Thomson multi-taper method. Dashed lines correspond to the PSD of a first-order autoregressive model fitted on the data. The peaks above the dashed lines are indicative of a difference from a red noise process. (b–e) Regression of precipitation (mm/day, shaded) and sea level pressure (hPa, contours) anomalies averaged in JFM and JJA for CMCC-CM2 and atmospheric data (GPCP for precipitation and ERA-Interim reanalysis for SLP), respectively. The anomalies correspond to 1 °C variation of the sea surface temperature index. For SLP the contours shown are −5, −4, −3, −2, −1.2, −0.9, −0.6, −0.3, 0.3, 0.6, 0.9, 1.2, 2 3, 4, and 5. PSD = Power Spectrum Density; CMCC-CM2 = Euro-Mediterranean Centre on Climate Change coupled climate model; JFM = January–March; JJA = June–August; GPCP = Global Precipitation Climatology Project.

Northern Hemisphere are associated with the broad-scale Asian summer monsoon (in the domain 60–130°E), the West African Monsoon (20°W to 40°E), and the North American monsoon (125–95°W; Figure 15b). These features are realistically represented, although they are underestimated in intensity over Asia and West Africa, and overestimated over Mexico (Figure 15a). Compared with the previous version of the model, improvements are noticeable over West Africa and North America monsoon regions where the strong simulated precipitation are now reduced (not shown). Over Asia instead the monsoon precipitation is weaker than observed (Cherchi et al., 2011) although the relative maxima over western India and Bay of Bengal are well captured. Negative values in the Southern Hemisphere represent the DJF peaks associated with the Australian monsoon, the South American monsoon system and the South African monsoon, respectively (Kitoh et al., 2013; Figure 15b). These patterns are realistically reproduced both in terms of intensity and spatial extent (Figure 15a). Compared with the previous version of the CMCC model monsoon intensities over North Australia and South Africa are better represented (Cherchi et al., 2011). Over South America, instead,

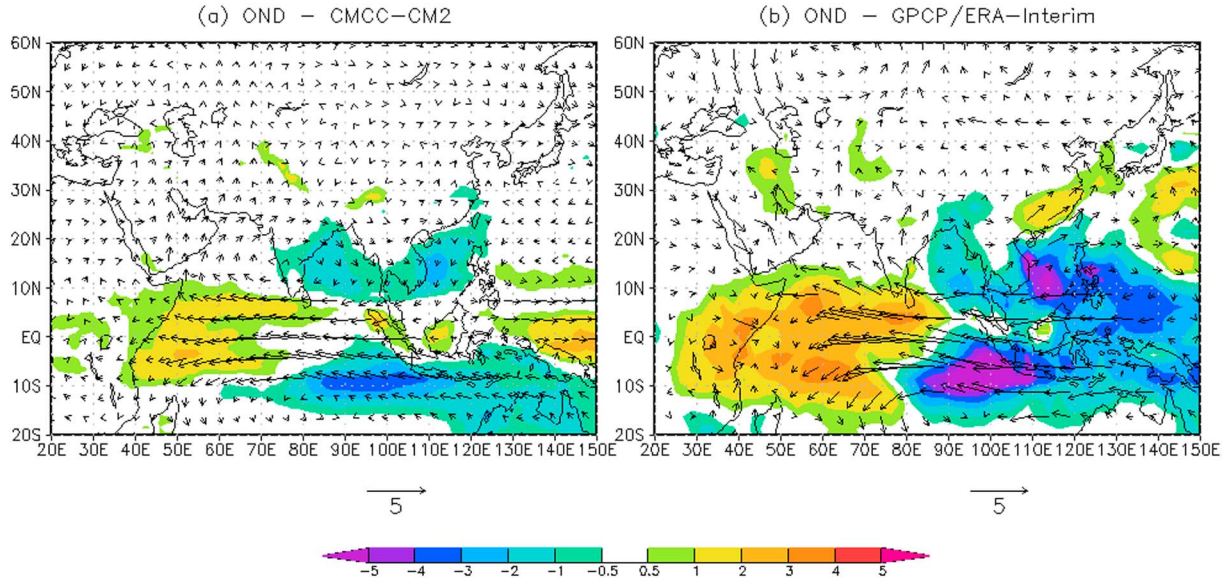

Figure 14. Regression of precipitation (mm/day, shaded) and wind at 850 hPa (m/s, vectors) anomalies averaged in OND for (a) CMCC-CM2 and (b) atmospheric data (GPCP for precipitation and ERA-Interim reanalysis for winds), respectively, on IOD index. The anomalies correspond to 1 °C variation of the IOD index. CMCC-CM2 = Euro-Mediterranean Centre on Climate Change coupled climate model; GPCP = Global Precipitation Climatology Project; IOD = Indian Ocean Dipole; OND = October-November-December.

the model performance deteriorates with respect to the previous version, as the peak over Northeastern Brazil (nordeste) is not anymore reproduced (Figure 15a), likely because of the strong precipitation deficit there (as described in previous sections).

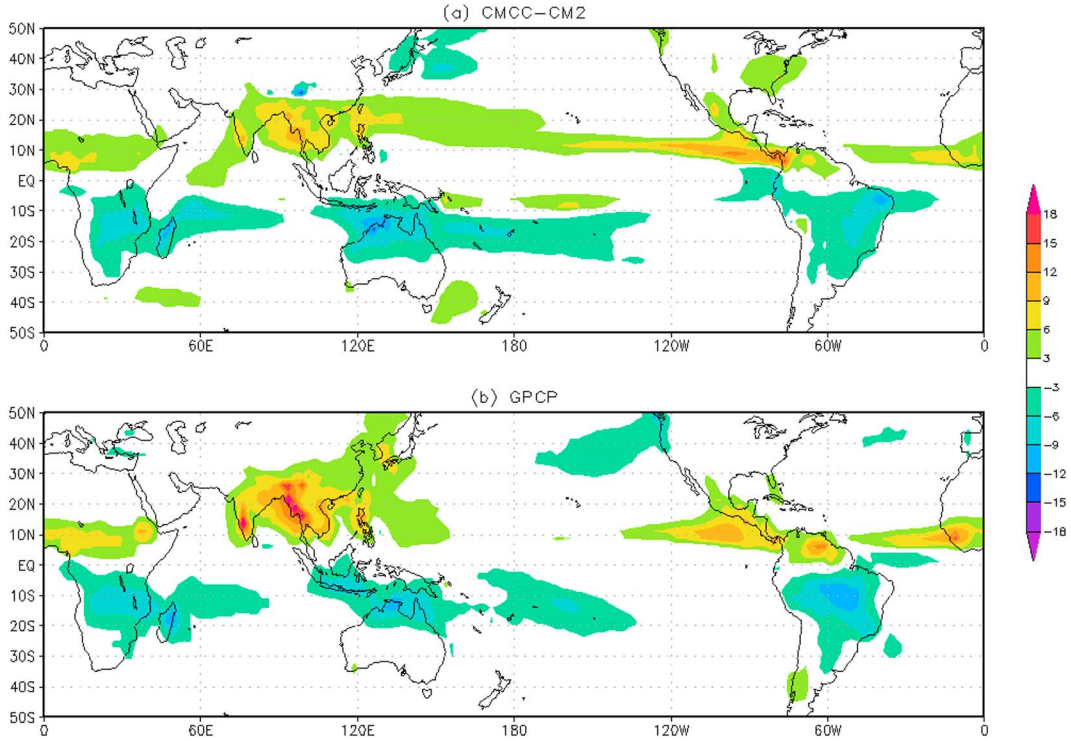

Figure 15. Global summer monsoon domains in terms of June–August minus December–February mean precipitation (mm/day) for (a) CMCC-CM2 and (b) GPCP. CMCC-CM2 = Euro-Mediterranean Centre on Climate Change coupled climate model; GPCP = Global Precipitation Climatology Project.

5. Conclusions

CMCC-CM2 represents the new family of the global coupled climate models developed and used at CMCC. It is based on the atmospheric, land, and sea ice components from the CESM (NCAR) climate model coupled to the global ocean model NEMO. This new coupling is the specific mark of the new family of coupled models in use at CMCC, and it represents the main novelty of the CMCC models. In this study we document the performance of the standard version of the model, CMCC-CM2-SR5, in terms of mean climate and main patterns of interannual variability. This specific configuration consists of the atmospheric component CAM5, the land components CLM4.5, and the sea ice component CICE4 coupled with the global ocean model NEMO (version 3.6). Other versions of the model are available at CMCC to address different needs, like seasonal prediction purposes or Earth System model issues, as well as to participate to different MIPs within the upcoming CMIP6. In particular, for HighResMIP (Haarsma et al., 2016) ad hoc versions of CMCC-CM2 have been implemented, using CAM4 with a prescribed anthropogenic aerosols formulation (Stevens et al., 2017) at two different horizontal resolutions (1° and ¼°), coupled to an eddy-permitting (1/4°) NEMO ocean configuration. A version of the CMCC model at high-resolution has been recently tested in a short experiment in terms of tropical cyclones coupling processes (Scoccimarro et al., 2017).

The experiment analyzed in this work consists of a 200-year present-day simulation with constant forcing held fixed at year 2,000 conditions. The system can be considered at the equilibrium with realistic balance at the top of the atmosphere and no drifts at the surface.

In terms of mean climate, the model is able to realistically reproduce the main patterns of temperature, precipitation, and winds. In terms of mean circulation, CMCC-CM2 provides a remarkable performance in the representation of upper tropospheric wind and midtroposphere geopotential eddies with positive implications for the representation of the main teleconnection patterns and future climate change scenarios. Specifically, we document improvements in the representation of the SST with respect to previous versions of the model. Improvements are also reported with respect to a CESM model configuration, differing for the ocean component, in some aspects of the annual SST, based on an indirect comparison with an experiment carried out using a similar setup (Small et al., 2014). The main differences (mostly in the Pacific and Indian Oceans) are likely to be ascribed to the different ocean model and should be analyzed in more detail with specific and coordinated experiments so as to identify possible recipes for additional improvements. Apart from SST, ocean heat transport and the MOC are in good agreement with observations and estimates from ocean reanalyses. The sea ice patterns and associated seasonal variations are realistically reproduced in the model in both hemispheres. This result may increase confidence in future sea ice projections and related climate. The most significant deficiencies relate to the cold bias affecting the high-latitude Northern Hemispheric 2-m temperatures over land, and the precipitation patterns, specifically in the tropical region, showing large dry biases over South America (Amazon basin). The seasonal precipitation associated with the monsoon systems, mostly over Asia, is weaker than observed. The position of the ITCZ is realistic in the model even though the intensity is more intense than the observed one, and overall, the simulated annual mean precipitation zonally averaged is overestimated with unrealistic peaks in the Southern Hemisphere close to the equator (double-ITCZ syndrome) and in the Southern Hemisphere at middle-to-high latitudes.

The seasonal march of SST along the equator, an indicator of the equatorial and tropical dynamics, is realistic in the model, mostly in the Pacific Ocean where the timing of the annual cycle is well reproduced even though the anomalies extend too westward. In the Atlantic Ocean the bias with large anomalies located toward the center of the basin are associated with the lack of upwelling along the eastern basin. In the Indian Ocean, the timing of the annual cycle is not well reproduced, as intense SST peaks occur in winter but they are not found in HadISST.

The interannual variability is realistic in the model, with a good representation of the main patterns of variability mostly in the Northern Hemisphere winter. NAM and PNA are well represented in the model with high spatial correlation with the observed patterns computed in terms of EOFs of SLP and geopotential height at 500 hPa, respectively. In the Southern Hemisphere the annular feature typical of the SAM computed in terms of austral winter EOFs of SLP is reproduced, but the maxima are not realistically located. In the tropics the main teleconnection patterns associated with ENSO and with the IOD are also well reproduced, with realistic precipitation, surface winds, and sea level pressure anomalies associated with NINO3.4 and the IOD SST index.

This work describes the main characteristics of the CMCC-CM2 family of climate models, introducing for the first time the coupling between the Community Ocean Model NEMO, largely used in Europe, and the atmospheric, land, and sea ice components of the CESM developed at NCAR. In particular, in this study we have shown the performance in terms of mean climate and main patterns of interannual variability of the standard version of the model (i.e., CMCC-CM2-SR5) with CAM5 as atmospheric model and the horizontal resolution of atmosphere and ocean at 1°. This first validation will be corroborated with more specific and dedicated (process-oriented) analyses in the coming months, once the experiments scheduled in the framework of the upcoming CMIP6 effort will become available.

Acknowledgments
We are grateful to the two anonymous reviewers whose instructive comments largely helped in improving the manuscript. The experiment analyzed has been performed on the Athena supercomputer at the Foundation Euro-Mediterranean Centre on Climate Change (CMCC). Outputs of the experiment used are stored in the data server of CMCC. The data and scripts used to build the figures in the manuscript are available as gzipped files in the supporting information. Other outputs of the experiment analyzed can be available upon request to the corresponding author (Annalisa Cherchi: annalisa.cherchi@ingv.it). This work has received funding from the European Union's Horizon 2020 research and innovation programme under Grant 641816 (CRESCENDO) and by the PRIMAVERA project funded by the European Union's Horizon 2020 programme, Grant 641727.

References

Adler, R. F., Huffman, G. J., Chang, A., Ferraro, R., Xie, P., Janowiak, J., et al. (2003). The version 2 Global Precipitation Climatology Project (GPCP) monthly precipitation analysis (1979–present). *Journal of Hydrometeorology*, *4*(6), 1147–1167. https://doi.org/10.1175/1525-7541(2003)004<1147:TVGPCP>2.0.CO;2

Albani, S., Mahowald, N. M., Perry, A. T., Scanza, R. A., Zender, C. S., Heavens, N. G., et al. (2014). Improved dust representation in the Community Atmosphere Model. *Journal of Advances in Modeling Earth Systems*, *6*, 541–570. https://doi.org/10.1002/2013MS000279

Annamalai, H., Taguchi, B., McCreary, J. P., Nagura, M., & Miyama, T. (2017). Systematic errors in South Asian monsoon simulation: Importance of equatorial Indian Ocean processes. *Journal of Climate*, *30*(20), 8159–8178. https://doi.org/10.1175/JCLI-D-16-0573.1

Arndt, J. E., Schenke, H. W., Jakobsson, M., Nitsche, F. O., Buys, G., Goleby, B., et al. (2013). The International Bathymetric Chart of the Southern Ocean 15 (IBCSO) version 1.0—A new bathymetric compilation covering circum-Antarctic waters. *Geophysical Research Letters*, *40*, 3111–3117. https://doi.org/10.1002/grl.50413

Ashok, K., Guan, Z., Saji, N. H., & Yamagata, T. (2001). Impact of the Indian Ocean dipole on the relationship between the Indian monsoon rainfall and ENSO. *Geophysical Research Letters*, *28*(23), 4499–4502. https://doi.org/10.1029/2001GL013294

Athanasiadis, P., Bellucci, A., Scaife, A., Hermanson, L., Materia, S., Sanna, A., et al. (2017). A multi-system view of wintertime NAO seasonal predictions. *Journal of Climate* https://doi.org/10.1175/JCLI-D-16-0153.1, *30*(4), 1461–1475.

Barnston, A. G., & Livezey, R. E. (1987). Classification, seasonality and persistence of low-frequency atmospheric circulation patterns. *Monthly Weather Review*, *115*(6), 1083–1126. https://doi.org/10.1175/1520-0493(1987)115<1083:CSAPOL>2.0.CO;2

Behera, S. K., Luo, J.-J., Masson, S., Delecluse, P., Gualdi, S., Navarra, A., & Yamagata, T. (2005). Paramount impact of the Indian Ocean Dipole on the East African short rains: A CGCM study. *Journal of Climate*, *18*(21), 4514–4530. https://doi.org/10.1175/JCLI3541.1

Bellucci, A., Gualdi, S., & Navarra, A. (2010). The double-ITCZ syndrome in coupled general circulation models: The role of large-scale vertical circulation regimes. *Journal of Climate*, *23*(5), 1127–1145. https://doi.org/10.1175/2009JCLI3002.1

Bellucci, A., Gualdi, S., Scoccimarro, E., & Navarra, A. (2008). NAO–ocean circulation interactions in a coupled general circulation model. *Climate Dynamics*, *31*(7-8), 759–777. https://doi.org/10.1007/s00382-008-0408-4

Bitz, C. M., & Lipscomb, W. H. (1999). An energy-conserving thermodynamic model of sea-ice. *Journal of Geophysical Research*, *104*(C7), 15669–15677. https://doi.org/10.1029/1999JC900100

Blanke, B., & Delecluse, P. (1993). Variability of the tropical Atlantic Ocean simulated by a general circulation model with two different mixed layer physics. *Journal of Physical Oceanography*, *23*(7), 1363–1388. https://doi.org/10.1175/1520-0485(1993)023<1363:VOTTAO>2.0.CO;2

Bogenschutz, P. A., Gettelman, A., Hannay, C., Larson, V. E., Neale, R. B., Craig, C., & Chen, C. C. (2018). The path to CAM6: Coupled simulations with CAM5.4 and CAM5.5. *Geoscientific Model Development*, *11*, 1–38. https://doi.org/10.5194/gmd-2017-129

Bonan, G. B., Lawrence, P. J., Oleson, K. W., Levis, S., Jung, M., Reichstein, M., et al. (2011). Improving canopy processes in the Community Land Model (CLM4) using global flux fields empirically inferred from FLUXNET data. *Journal of Geophysical Research*, *116*, G02014. https://doi.org/10.1029/2010JG001593

Branstetter ML (2001) Development of a parallel river transport algorithm and applications to climate studies. Ph.D. dissertation, University of Texas at Austin.

Branstetter, M. L., & Famiglietti, J. S. (1999). Testing the sensitivity of GCM-simulated runoff to climate model resolution using a parallel river transport algorithm. Preprints, 14th Conference on Hydrology, Dallas, TX, Amer. Meteor. Soc., 391–392.

Bretherthon, C. S., & Park, S. (2009). A new moist turbulence parameterization in the community atmosphere model. *Journal of Climate*, *22*(12), 3422–3448. https://doi.org/10.1175/2008JCLI2556.1

Briegleb, B., & Light, B. (2007). A Delta-Eddigton multiple scattering parameter for solar radiation in the sea ice component of the Community Climate System Model. *NCAR Technical Note*, NCAR/TN-472+ STR, National Center for Atmospheric Research. https://doi.org/10.5065/D6B27S71

Chang, P. (1994). A study of the seasonal cycle of sea surface temperature in the tropical Pacific Ocean using reduced gravity models. *Journal of Geophysical Research*, *99*(C4), 7725–7741. https://doi.org/10.1029/93JC03561

Charlton-Perez, A. J., Baldwin, M. P., Birner, T., Black, R. X., Butler, A. H., Calvo, N., et al. (2013). On the lack of stratospheric dynamical variability in low-top versions of the CMIP5 models. *Journal of Geophysical Research: Atmospheres*, *118*, 2494–2505. https://doi.org/10.1002/jgrd.50125

Cherchi, A., Alessandri, A., Masina, S., & Navarra, A. (2011). Effects of increased CO_2 levels on monsoons. *Climate Dynamics*, *37*(1-2), 83–101. https://doi.org/10.1007/s00382-010-0801-7

Cherchi, A., Masina, S., & Navarra, A. (2008). Impact of extreme CO_2 levels on tropical mean climate: A CGCM study. *Climate Dynamics*, *31*(7–8), 743–758. https://doi.org/10.1007/s00382-008-0414-6

Craig, A. P., Vertenstein, M., & Jacob, R. (2012). A new flexible coupler for Earth system modeling developed for CCSM4 and CESM1. *International Journal of High Performance Computing*, *26*(1), 31–42. https://doi.org/10.1177/1094342011428141

Cunningham, S. A., Kanzow, T., Rayner, D., Baringer, M. O., Johns, W. E., Marotzke, J., et al. (2007). Temporal variability of the Atlantic Meridional Overturning circulation at 26.5N. *Science*, *317*, 935–938.

Danabasoglu, G., Yeager, S. G., Bailey, D., Behrens, E., Bentsen, M., Bi, D., et al. (2014). North Atlantic simulations in Coordinated Ocean-ice Reference Experiments phase II (CORE-II). Part I: Mean states. *Ocean Modelling*, *73*, 76–107. https://doi.org/10.1016/j.ocemod.2013.10.005

Dee, D. P., Uppala, S. M., Simmons, A. J., Berrisford, P., Poli, P., Kobayashi, S., et al. (2011). The ERA-Interim re-analysis: Configuration and performance of the data assimilation system. *Quarterly Journal of the Royal Meteorological Society*, *137*(656), 553–597. https://doi.org/10.1002/qj.828

Delworth, T. L., Rosati, A., Anderson, W., Adcroft, A. J., Balaji, V., Benson, R., et al. (2012). Simulated climate and climate change in the GFDL CM2.5 high-resolution coupled climate model. *Journal of Climate*, *25*(8), 2755–2781. https://doi.org/10.1175/JCLI-D-11-00316.1

Dijkstra, H. A., & Neelin, D. J. (1995). Ocean-atmosphere interaction and the tropical climatology. Part II: Why the Pacific cold tongue is in the east. *Journal of Climate*, *8*(5), 1343–1359. https://doi.org/10.1175/1520-0442(1995)008<1343:OAIATT>2.0.CO;2

Eyring, V., Bony, S., Meehl, G. A., Senior, C. A., Stevens, B., Stouffer, R. J., & Taylor, K. E. (2016). Overview of the Coupled Model Intercomparison Project Phase 6 (CMIP6) experimental design and organization. *Geoscientific Model Development*, *9*, 1937–1958. https://doi.org/10.5194/gmd-9-1937-2016

Fetterer, F., Meier, W., Savoie, M, & Windnagel, A. (2008). Sea ice index. NSIDC report https://nsidc.org/data/g02135?qt-data_set_tabs=2#qt-data_set_tabs.

Fofonoff, N., & Millard, R. (1983). Algorithms for computation of fundamental property of sea water. UNESCO Techn. Paper in Mar. Sci, 44, (53 pp.).

Fogli, P. G., & Iovino, D. (2014). CMCC-CESM-NEMO: Toward the new CMCC Earth System Model. CMCC Research Papers RP0248.

Gettelman, A., Morrison, H., & Ghan, S. J. (2008). A new two-moment bulk stratiform cloud microphysics scheme in the NCAR Community Atmosphere Model (CAM3). Part II: Single-column and global results. *Journal of Climate*, *21*(15), 3660–3679. https://doi.org/10.1175/2008JCLI2116.1

Gualdi, S., Scoccimarro, E., & Navarra, A. (2008). Changes in tropical cyclone activity due to global warming: Results from a high-resolution coupled general circulation model. *Journal of Climate*, *21*(20), 5204–5228. https://doi.org/10.1175/2008JCLI1921.1

Haarsma, R. J., Roberts, M. J., Vidale, P. L., Senior, C. A., Bellucci, A., Bao, Q., et al. (2016). High Resolution Model Intercomparison Project (HighResMIP v1.0) for CMIP6. *Geoscientific Model Development*, *9*(11), 4185–4208. https://doi.org/10.5194/gmd-9-4185-2016

Hall, A., & Qu, X. (2006). Using the current seasonal cycle to constrain snow albedo feedback in future climate change. *Geophysical Research Letters*, *33*, L03502. https://doi.org/10.1029/2005GL025127

Harris, I. C., & Jones, P. D. (2017). CRU TS4.00: Climatic Research Unit (CRU) Time-Series (TS) version 4.00 of high resolution gridded data of month-by-month variation in climate (Jan. 1901–Dec. 2015). Centre for Environmental Data Analysis, 25 May 2017.

Hastenrath, S., Nicklis, A., & Greischar, L. (1993). Atmospheric-hydrospheric mechanisms of climate anomalies in the western equatorial Indian Ocean. *Journal of Geophysical Research*, *98*, 20,219–20,235.

Hendon, H. H., Thompson, D. W., & Wheeler, M. C. (2007). Australian rainfall and surface temperature variations associated with the Southern Hemisphere annular mode. *Journal of Climate*, *20*(11), 2452–2467. https://doi.org/10.1175/JCLI4134.1

Hewitt, H. T., Roberts, M. J., Hyder, P., Graham, T., Rae, J., Belcher, S. E., et al. (2016). The impact of resolving the Rossby radius at mid-latitudes in the ocean: Results from a high-resolution version of the Met Office GC2 coupled model. *Geoscientific Model Development*, *9*(10), 3655–3670. https://doi.org/10.5194/gmd-9-3655-2016

Holland, M. M., Bailey, D. A., Briegleb, B. P., Light, B., & Hunke, E. (2012). Improved sea ice shortwave radiation physics in CCSM4: The impact of melt ponds and aerosols on Arctic sea ice. *Journal of Climate*, *25*(5), 1413–1430. https://doi.org/10.1175/JCLI-D-11-00078.1

Hsu, P. C., Li, T., Murakami, H., & Kitoh, A. (2013). Future change of the global monsoon revealed from 19 CMIP5 models. *Journal of Geophysical Research: Atmospheres*, *118*, 1247–1260. https://doi.org/10.1002/jgrd.50145

Hunke, E., & Lipscomb, W. (2008). CICE: The Los Alamos sea ice model, documentation and software, version 4.0. Los Alamos National Laboratory, Technical Report LA-CC-06-012

Hunke, E. C., & Dukowicz, J. K. (2002). The elastic-viscous-plastic sea ice dynamics model in general orthogonal curvilinear coordinates on a sphere-incorporation of metric terms. *Monthly Weather Review*, *130*(7), 1848–1865. https://doi.org/10.1175/1520-0493(2002)130<1848:TEVPSI>2.0.CO;2

Hurrell, J., Kushnir, Y., Ottersen, G., & Visbeck, M. (2003). An overview of the North Atlantic Oscillation. In J. Hurrell, J. Kushnir, G. Ottersen, & M. Visbeck (Eds.), *The North Atlantic Oscillation: Climatic significance and environmental impact* (pp. 1–35). Washington DC: American Geophysical Union. https://doi.org/10.1029/134GM01

Hurrell, J. W. (1995). Decadal trends in the North Atlantic Oscillation: Regional temperatures and precipitation. *Science*, *269*(5224), 676–679 https://doi.org/10.1126/science.269.5224.676.

Hwang, Y. T., & Frierson, D. M. W. (2013). Link between the double-Intertropical Convergence Zone problem and cloud biases over the Southern Ocean. *PNAS*, *110*(13), 4935–4940. https://doi.org/10.1073/pnas.1213302110

Iacono, M., Delamere, J., Mlawer, E., Shephard, M., Clough, S., & Collins, W. (2008). Radiative forcing by long-lived greenhouse gases: Calculations with the AER radiative transfer models. *Journal of Geophysical Research*, *113*, D13103. https://doi.org/10.1029/2008JD009944

Iovino, D., Masina, S., Storto, A., Cipollone, A., & Stepanov, V. N. (2016). A 1/16° eddying simulation of the global NEMO sea-ice-ocean system. *Geoscientific Model Development*, *9*(8), 2665–2684. https://doi.org/10.5194/gmd-9-2655-2016

Jones, P. D., Lister, D. H., Osborn, T. J., Harpham, C., Salmon, M., & Morice, P. (2012). Hemispheric and large-scale land-surface air temperature variations: An extensive revision and an update to 2010. *Journal of Geophysical Research*, *117*, D05127. https://doi.org/10.1029/2011JD017139

Kitoh, A., Endo, H., Kumar, K. K., Cavalcanti, I. F. A., Goswami, P., & Zhou, T. (2013). Monsoons in a changing world: A regional perspective in a global context. *Journal of Geophysical Research: Atmospheres*, *118*, 3053–3065. https://doi.org/10.1002/jgrd.50258

Kok, J. F., Ridley, D. A., Zhou, Q., Miller, R. L., Zhao, C., Heald, C. L., et al. (2017). Smaller desert dust cooling effect estimated from analysis of dust size and abundance. *Nature Geoscience*, *10*(4), 274–278. https://doi.org/10.1038/ngeo2912

Koven, C. D., Riley, W. J., Subin, Z. M., Yang, J. Y., Torn, M. S., Collins, W. D., et al. (2013). The effect of vertically resolved soil biogeochemistry and alternate soil C and N models on C dynamics of CLM4. *Biogeosciencies*, *10*(11), 7109–7131 https://doi.org/10.5194/bg-10-7109-2013.

Langenbrunner, B., & Neelin, J. D. (2013). Analyzing ENSO teleconnections in CMIP models as a measure of model fidelity in simulating precipitation. *Journal of Climate*, *26*(13), 4431–4446. https://doi.org/10.1175/JCLI-D-12-00542.1

Large, W. G., & Danabasoglu, G. (2006). Attribution and impacts of upper-ocean biases in CCSM3. *Journal of Climate*, *19*(11), 2325–2346. https://doi.org/10.1175/JCLI3740.1

Lauritzen, P. H., Bacmeister, J. T., Callaghan, P. F., & Taylor, M. A. (2015). NCAR global model topography generation software for unstructured grids. *Geoscientific Model Development Discussion*, *8*(6), 4623–4651. https://doi.org/10.5194/gmdd-8-4623-2015

Lengaigne, M., Menkes, C., Aumont, O., Gorgues, T., Bopp, L., & Madec, J.-M. A. G. (2007). Biophysical feedbacks on the tropical pacific climate in a coupled general circulation model. *Climate Dynamics*, *28*, 503–516.

Li, F., Bond-Lamberty, B., & Levis, S. (2014). Quantifying the role of fire in the Earth system—Part 2: Impact on the net carbon balance of global terrestrial ecosystems for the 20th century. *Biogeosciencies*, *11*(5), 1345–1360 https://doi.org/10.5194/bg-11-1345-2014.

Li, F., Levis, S., & Ward, D. S. (2013). Quantifying the role of fires in the Earth system—Part I: Improved global fire modeling in the Community Earth System Model (CESM1). *Biogeosciencies*, *10*(4), 2293–2314. https://doi.org/10.5194/bg-10-2293-2013

Li, F., Zeng, X. D., & Levis, S. (2012). A process based fire parameterization of intermediate complexity in a Dynamic Global Vegetation Model. *Biogeosciencies*, *9*(7), 2761–2780. https://doi.org/10.5194/bg-9-2761-2012

Lin, S. J., & Rood, R. B. (1996). Multi-dimensional flux from semi-Lagrangian transport schemes. *Monthly Weather Review*, *124*(9), 2046–2070. https://doi.org/10.1175/1520-0493(1996)124<2046:MFFSLT>2.0.CO;2

Liu, X., Easter, R. C., Ghan, S. J., Zaveri, R., Rasch, P. J., Shi, X., et al. (2012). Toward a minimal representation of aerosols in climate models: Description and evaluation in the community atmosphere model CAM5. *Geoscientific Model Development*, *5*(3), 709–739. https://doi.org/10.5194/gmd-5-709-2012

Locarnini, R. A., Mishonov, A. V., Antonov, J. I., Boyer, T. P., Garcia, H. E., Baranova, O. K., et al. (2013). World Ocean Atlas 2013, Volume 1: Temperature. S. Levitus, Ed., A. Mishonov Technical Ed.; NOAA Atlas NESDIS 73, 40 pp.

Madec, G., & Imbard, M. (1996). A global ocean mesh to overcome the North Pole singularity. *Climate Dynamics*, *12*, 381–388.

Madec, G., & the NEMO team (2016). NEMO ocean engine—Version 3.6. Tech Rep ISSN 1288–1619 No 27 Pôle de Modélisation, Institut Pierre-Simon Laplace (IPSL), France

Marshall, J., Donohoe, A., Ferreira, D., & McGee, D. (2014). The ocean's role in setting the mean position of the Inter-Tropical Convergence Zone. *Climate Dynamics*, *42*(7-8), 1967–1979. https://doi.org/10.1007/s00382-013-1767-z

Martins, G., von Randow, C., Sampaio, G., & Dolman, A. J. (2015). Precipitation in the Amazon and its relationship with moisture transport and tropical Pacific and Atlantic SST from the CMIP5 simulation. *Hydrology and Earth System Sciences Discuss*: https://doi.org/10.5194/hessd-12-671-2015, *12*(1), 671–704.

Masina, S., Storto, A., Ferry, N., Valdivieso, M., Haines, K., Balmaseda, M., et al. (2017). An ensemble of eddy-permitting global ocean reanalyses from the MyOcean project. *Climate Dynamics*, *49*(3), 813–841.

McCarthy, G. D., Smeed, D. A., Johns, W. E., Frajka-Williams, E., Moat, B. I., Rayner, D., et al. (2015). Measuring the Atlantic meridional over-turning circulation at 26N. *Progress in Oceanography*, *130*, 91–111. https://doi.org/10.1016/j.pocean.2014.10.006

Mechoso, C. R., Robertson, A. W., Barth, N., Davey, M. K., Delecluse, P., Gent, P. R., et al. (1995). The seasonal cycle over the Tropical Pacific in coupled ocean-atmosphere general circulation models. *Monthly Weather Review*, *123*(9), 2825–2838. https://doi.org/10.1175/1520-0493(1995)123<2825:TSCOTT>2.0.CO;2

Meehl, G. A., Covey, C., Delworth, T., Latif, M., McAvaney, B., Mitchell, J. R. B., et al. (2007). The WCRP CMIP3 mutimodel dataset: A new era in climate change research. *Bulletin of the American Meteorological Society*, *88*(9), 1383–1394. https://doi.org/10.1175/BAMS-88-9-1383

Mitchell, T. P., & Wallace, J. M. (1992). The annual cycle in equatorial convection and sea surface temperature. *Journal of Climate*, *5*(10), 1140–1156. https://doi.org/10.1175/1520-0442(1992)005<1140:TACIEC>2.0.CO;2

Mo, K. C., & Paegle, J. N. (2001). The Pacific-South American modes and their downstream effects. *International Journal of Climatology*, *21*(10), 1211–1229. https://doi.org/10.1002/joc.685

Morgenstern, O., Braesicke, P., O'Connor, F. M., Bushell, A. C., Johnson, C. E., Osprey, S. M., & Pyle, J. A. (2009). Evaluation of the new UKCA climate-composition model. Part 1: The stratosphere. *Geoscientific Model Development*, *2*(1), 43–57. https://doi.org/10.5194/gmd-2-43-2009

Neale, R., Conley, A. J., Garcia, R., Kinnison, D., Lamarque, J. F., Marsh, D., et al. (2012) Description of the NCAR Community Atmosphere Model (CAM5.0). NCAR/TN-486+STR, NCAR Technical Note (http://www.cesm.ucar.edu/models/cesm1.0/cam/docs/description/cam5_desc.pdf)

Neale, R. B., Richter, J. H., Conley, A. J., Park, S., Lauritzen, P. H., Gettelman, A., et al. (2010). Description of the NCAR Community Atmosphere Model (CAM4.0). NCAR/TN-485+STR, NCAR Technical Note

Nigam, S., & Chao, Y. (1996). Evolution dynamics of tropical ocean-atmosphere annual cycle variability. *Journal of Climate*, *9*(12), 3187–3205. https://doi.org/10.1175/1520-0442(1996)009<3187:EDOTOA>2.0.CO;2

NOAA (2006). https://www.ngdc.noaa.gov/mgg/global/etopo2.html

Oleson, K. W., Lawrence, D. M., Bonan, G. B., Drewniak, B., Huang, M., Koven, C. D., et al. (2013). Technical description of version 4.5 of the Community Land Model (CLM). NCAR Technical Note, NCAR/TN-503+STR

Park, S., & Bretherton, C. S. (2009). The University of Washington shallow convection and moist turbulence schemes and their impact on climate simulations with the community atmosphere model. *Journal of Climate*, *22*(12), 3449–3469. https://doi.org/10.1175/2008JCLI2557.1

Park, S., Bretherton, C. S., & Rasch, P. J. (2014). Integrating cloud processes in the Community Atmosphere Model, version 5. *Journal of Climate*, *27*(18), 6821–6856. https://doi.org/10.1175/JCLI-D-14-00087.1

Parton, W., Stewart, J., & Cole, C. (1988). Dynamics of C, N, P and S in grassland soils—A model. *Biogeochemistry*, *5*(1), 109–131. https://doi.org/10.1007/BF02180320

Philander, S. G. H., & Pacanowski, R. C. (1981). The oceanic response to cross-equatorial winds (with application to coastal upwelling in low latitudes). *Tellus*, *33*, 201–210.

Pithan, F., Shepherd, T. G., Zappa, G., & Sandu, I. (2016). Climate model biases in jet streams, blocking and storm tracks resulting from missing orographic drag. *Geophysical Research Letters*, *43*, 7231–7240. https://doi.org/10.1002/2016GL069551

Rackow, T., Goessling, H. F., Jung, T., Sidorenko, D., Semmler, T., Barbi, D., & Handorf, D. (2018). Towards multi-resolution global climate modelling with ECHAM6-FESOM. Part II: Climate variability. *Climate Dynamics*, *50*, 2369–2394.

Rayner, N. A., Parker, D. E., Horton, E. B., Folland, C. K., Alexander, L. V., Rowell, D. P., et al. (2003). Global analyses of sea surface temperature, sea ice, and night marine air temperature since the late nineteenth century. *Journal of Geophysical Research*, *108*(D14), 4407. https://doi.org/10.1029/2002JD002670

Richter, I. (2015). Climate model biases in the eastern tropical oceans: Causes, impacts and ways forward. *Wiley Interdisciplinary Reviews: Climate Change*, *6*(3), 345–358.

Richter, J. H., Solomon, A., & Bacmeister, J. T. (2014). Effects of vertical resolution and nonorographic gravity wave drag on the simulated climate in the Community Atmosphere Model, version 5. *Journal of Advances in Modeling Earth Systems*, *6*, 357–383. https://doi.org/10.1002/2013MS000303

Rogers, J. C., & van Loon, H. (1982). Spatial variability of sea level pressure and 500-mb height anomalies over the southern hemisphere. *Monthly Weather Review*, *110*(10), 1375–1392. https://doi.org/10.1175/1520-0493(1982)110<1375:SVOSLP>2.0.CO;2

Rothrock, D. (1975). The energetics of the plastic deformation of pack ice by ridging. *Journal of Geophysical Research*, *80*(33), 4514–4519. https://doi.org/10.1029/JC080i033p04514

Roullet, G., & Madec, G. (2000). Salt conservation, free surface and varying levels: A new formulation for ocean general circulation models. *Journal of Geophysical Research*, *105*(C10), 23927–23942. https://doi.org/10.1029/2000JC900089

Saji, N. H., Goswami, B. N., Vinaychandran, P. N., & Yamagata, T. (1999). A dipole mode in the tropical Indian Ocean. *Nature*, *401*(6751), 360–363. https://doi.org/10.1038/43854

Sanna, A., Borrelli, A., Materia, S., Athanasiadis, P., Bellucci, A., Fogli, P. G., et al. (2015). The new CMCC—Seasonal prediction system. CMCC Research Papers RP0253 13 pp.

Scaife, A. A., Arribas, A., Blockley, E., Brookshaw, A., Clark, R. T., Dunstone, N., et al. (2014). Skillful long-range prediction of European and North American winters. *Geophysical Research Letters*, *41*, 2514–2519. https://doi.org/10.1002/2014GL059637

Schott, F., & McCreary, J. P. (2001). The monsoon circulation of the Indian Ocean. *Progress in Oceanography*, *51*(1), 1–123. https://doi.org/10.1016/S0079-6611(01)00083-0

Scoccimarro, E., Fogli, P. G., Reed, K., Gualdi, S., Masina, S., & Navarra, A. (2017). Tropical cyclone interaction with the ocean: The role of high-frequency (sub-daily) coupled processes. *Journal of Climate*: https://doi.org/10.1175/JCLI-D-16-0292.1, *30*(1), 145–162.

Scoccimarro, E., Gualdi, S., Bellucci, A., Sanna, A., Fogli, P. G., Manzini, E., et al. (2011). Effects of tropical cyclones on ocean heat transport in a high-resolution coupled general circulation model. *Journal of Climate*, *24*(16), 4368–4384. https://doi.org/10.1175/2011JCLI4104.1

Shepherd, T. G. (2014). Atmospheric circulation as a source of uncertainty in climate change projections. *Nature Geoscience*, *7*(10), 703–708. https://doi.org/10.1038/ngeo2253

Small, R. J., Justin Small, R., Bacmeister, J., Bailey, D., Baker, A., Bishop, S., et al. (2014). A new synoptic scale resolving global climate simulation using the Community Earth System Model. *Journal of Advances in Modeling Earth Systems*, *6*, 1065–1094. https://doi.org/10.1002/2014MS000363

Smoliak, B. V., & Wallace, J. M. (2015). On the leading patterns of Northern Hemisphere sea level pressure variability. *Journal of the Atmospheric Sciences*, *72*(9), 3469–3486. https://doi.org/10.1175/JAS-D-14-0371.1

Song, Z. Y., Liu, H. L., Zhang, C. Z., Zhang, L. P., & Qiao, F. L. (2014). Evaluation of the eastern equatorial Pacific SST seasonal cycle in CMIP5 models. *Ocean Science*, *10*(5), 837–843. https://doi.org/10.5194/os-10-837-2014

Stevens, B., Fiedler, S., Kinne, S., Peters, K., Rast, S., Müsse, J., et al. (2017). MACv2-SP: A parameterization of anthropogenic aerosol optical properties and an associated Twomey effect for use in CMIP6. *Geoscientific Model Development*, *10*, 433–452, https://doi.org/10.5194/gmd-10-433-2017.

Subin, Z. M., Riley, W. J., & Mironov, D. (2012). Improved lake model for climate simulations. *Journal of Advances in Modeling Earth Systems*, *4*, M020001. https://doi.org/10.1029/2011MS000072

Sun, Y., Gu, L., & Dickinson, R. E. (2012). A numerical issue in calculating the coupled carbon and water fluxes in a climate model. *Journal of Geophysical Research*, *117*, D22103. https://doi.org/10.1029/2012JD018059

Swenson, S. C., & Lawrence, D. M. (2012). A new fractional snow-covered area paramterization for the Community Land Model and its effect on the surface energy balance. *Journal of Geophysical Research*, *117*, D21107. https://doi.org/10.1029/2012JD018178

Swenson, S. C., Lawrence, D. M., & Lee, H. (2012). Improved simulation of the terrestrial hydrological cycle in permafrost regions by the Community Land Model. *Journal of Advances in Modeling Earth Systems*, *4*, M08002. https://doi.org/10.1029/2012MS000165

Taylor, K. E., Stouffer, R. J., & Meehl, G. A. (2012). An overview of CMIP5 and the experiment design. *Bulletin of the American Meteorological Society*, *93*(4), 485–498. https://doi.org/10.1175/BAMS-D-11-00094.1

Thompson, D. W., & Wallace, J. M. (2000). Annualar modes in the extratropical circulation. Part I: Month-to-month variability. *Journal of Climate*, *13*(5), 1000–1016. https://doi.org/10.1175/1520-0442(2000)013<1000:AMITEC>2.0.CO;2

Thorndike, A. S., Rothrock, D. A., Maykut, G. A., & Colony, R. (1975). The thickness distribution of sea ice. *Journal of Geophysical Research*, *80*(33), 4501–4513. https://doi.org/10.1029/JC080i033p04501

Trenberth, K. E., & Fasullo, J. T. (2008). An observational estimate of inferred energy divergence. *Journal of Physical Oceanography*, *38*(5), 984–999. https://doi.org/10.1175/2007JPO3833.1

Trenberth, K. E., Fasullo, J. T., & Balmaseda, M. A. (2014). Earth's energy imbalance. *Journal of Climate*, *27*(9), 3129–3144. https://doi.org/10.1175/JCLI-D-13-00294.1

Ummenhofer, C. C., Sen Gupta, A., Briggs, P. R., England, M. H., McIntosh, P. C., Meyers, G. A., et al. (2011). Indian and Pacific Ocean influences on southeast Australian drought and soil moisture. *Journal of Climate*, *24*(5), 1313–1336. https://doi.org/10.1175/2010JCLI3475.1

van Loon, H., & Rogers, J. C. (1978). The seesaw in winter temperatures between Greenland and northern Europe. Part I: General description. *Monthly Weather Review*, *106*(3), 296–310. https://doi.org/10.1175/1520-0493(1978)106<0296:TSIWTB>2.0.CO;2

Vancoppenolle, M., Bouillon, S., Fichefet, T., Goosse, H., Lecomte, O., Morales Maqueda, M. A., & Madec, G. (2012). LIM The Louvain-la-Neuve sea ice model. Note du Pôle de Modélisation de l'Institut Pierre-Simon Laplace 31 ISSN 1288–1619

Walker, G. T., & Bliss, E. W. (1932). World weather. *Memoirs of the Royal Meteorological Society*, *4*, 53–83.

Wang, B., & Ding, Q. (2008). Global monsoon: Dominant mode of annual variation in the tropics. *Dynamics of Atmospheres and Oceans*, *44*(3-4), 165–183. https://doi.org/10.1016/j.dynatmoce.2007.05.002

Wang, C., Zhang, L., Lee, S. K., Wu, L., & Mechoso, C. R. (2014). A global perspective on CMIP5 climate model biases. *Nature Climate Change*, *4*(3), 201–205. https://doi.org/10.1038/nclimate2118

Wang, L. C., Jin, F. F., & Wu, C. R. (2017). Dynamics of simulated Atlantic upwelling annual cycle in CMIP5 models. *Journal of Geophysical Research: Oceans*, *122*, 5774–5785. https://doi.org/10.1002/2017JC012781

Wang, L. C., Jin, F. F., Wu, C. R., & Hsu, H. H. (2017). Dynamics of upwelling annual cycle in the equatorial Atlantic Ocean. *Geophysical Research Letters*, *44*, 4737–4743. https://doi.org/10.1002/2017GL072588

Xie, S. P. (2004). The shape of continents, air-sea interaction and the rising branch of the Hadley circulation. In H. F. Diaz, & R. S. Bradley (Eds.), *The Hadley circulation: Past, present and future*, (pp. 121–252). Netherlands: Springer.

Yu, X., & McPhaden, M. J. (1999). Seasonal variability in the equatorial Pacific. *Journal of Physical Oceanography*, *29*(5), 925–947. https://doi.org/10.1175/1520-0485(1999)029<0925:SVITEP>2.0.CO;2

Zalesak, S. T. (1979). Fully multidimensional flux corrected transport for fluids. *Journal of Computational Physics*, *31*(3), 335–362. https://doi.org/10.1016/0021-9991(79)90051-2

Zappa, G., Shaffrey, L. C., & Hodges, K. I. (2013). The ability of CMIP5 models to simulate North Atlantic extra-tropical cyclones. *Journal of Climate*, *26*(15), 5379–5396. https://doi.org/10.1175/JCLI-D-12-00501.1

Zweng, M. M., Reagan, J. R., Antonov, J. I., Locarnini, R. A., Mishonov, A. V., Boyer, T. P., et al. (2013). World ocean atlas 2013. In S. Levitus (Ed.), A. Mishonov Technical Ed. *Salinity* (Vol. 2, 74, pp. 1–40). Silver Spring, MD: NOAA Atlas NESDIS.